

Optical Control of Slow Topological Electrons in Moiré Systems

Christopher Yang,¹ Iliya Esin,¹ Cyprian Lewandowski,^{1,2,3} and Gil Refael¹

¹*Department of Physics, IQIM, California Institute of Technology, Pasadena, CA 91125, USA*

²*National High Magnetic Field Laboratory, Tallahassee, Florida, 32310, USA*

³*Department of Physics, Florida State University, Tallahassee, Florida 32306, USA*

Floquet moiré materials possess optically-induced flat-electron bands with steady-states sensitive to drive parameters. Within this regime, we show that strong interaction screening and phonon bath coupling can overcome enhanced drive-induced heating. In twisted bilayer graphene (TBG) irradiated by a terahertz-frequency continuous circularly polarized laser, the extremely slow electronic states enable the drive to control the steady state occupation of high-Berry curvature electronic states. In particular, above a critical field amplitude, high-Berry-curvature states exhibit a slow regime where they decouple from acoustic phonons, allowing the drive to control the anomalous Hall response. Our work shows that the laser-induced control of topological and transport physics in Floquet TBG are measurable using experimentally available probes.

Introduction— Time-periodic fields can drive materials into exotic non-equilibrium phases [1–15], with unconventional transport and optical characteristics [16–23] controllable by external parameters. In laser-driven twisted bilayer graphene (TBG) [24–28], a flat-band regime with pronounced electron-electron interaction effects is accessible away from the magic angles [29]. Generating low-temperature Floquet states in such a regime requires cooling processes that compensate for strong drive-induced electron-electron heating. A common cooling solution involves coupling Floquet systems to low-temperature phonon baths [3, 30, 31].

We demonstrate that intrinsic electron-phonon coupling in TBG and Coulomb screening can stabilize low-temperature steady-states in Floquet TBG under terahertz (THz) frequency, circularly polarized laser drives. In this steady-state, the drive amplitude controls the filling of electronic states with large Berry curvature, resulting in a highly tunable anomalous conductivity σ_{xy} [16, 32–35] (Fig. 1(a-b)). The ability to tune the Floquet steady-state results from the unique slow electron regime in TBG where phonons travel faster than—and decouple from—many flat band electronic states [36, 37]. The drive strength controls electron velocities, tuning between an equilibrated electronic gas with finite σ_{xy} at low drive amplitudes and a decoupled electronic gas with reduced electron velocities and suppressed σ_{xy} at high drive amplitudes.

The system.—We begin by constructing the time-periodic, interacting Hamiltonian for laser-driven TBG near the charge neutrality point and at a twist angle θ . The single-particle effective Hamiltonian of undriven TBG is $\hat{H}_0 = \sum_{\mathbf{k}\nu\xi} E_{\mathbf{k}\nu}^{(\xi)} \hat{c}_{\mathbf{k}\nu}^{(\xi)\dagger} \hat{c}_{\mathbf{k}\nu}^{(\xi)}$, where $\hat{c}_{\mathbf{k}\nu}^{(\xi)\dagger}$ creates a Bloch state $|\xi\nu\mathbf{k}\rangle$ of crystal momentum \mathbf{k} , band ν , and energy $E_{\mathbf{k}\nu}^{(\xi)}$, in the vicinity of the valley index $\xi = \pm 1$ of the single-layer graphene Brillouin zone [29, 41]. The index $\nu = \pm$ labels the central particle and hole bands (Fig. 2(a, b)) with total bandwidth W . These central bands are separated by a large energy gap from all other bands.

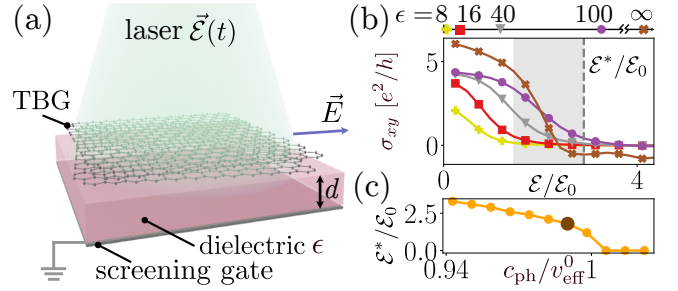


FIG. 1. (a) Schematic experimental design. Circularly polarized laser induces non-trivial Berry-curvature in the driven flat-bands, resulting in an anomalous Hall conductivity σ_{xy} . A dielectric and metallic gate screen Coulomb interactions. (b) Anomalous Hall conductivity vs. drive amplitude \mathcal{E} for various dielectric constants ϵ and a gate distance of $d = 13$ nm. The conductivity features a rapid drop (shaded) with \mathcal{E} below the critical amplitude \mathcal{E}^* (dashed line). Here, $\mathcal{E}_0 = \hbar v_F L_M^{-1} / (e L_M) = 7.177 \times 10^4$ V/m. (c) The critical amplitude vs. c_{ph}/v_{eff}^0 , where $v_{eff}^0 = v_{eff}(0)$ is an effective electron velocity defined in the text. The enlarged red circle denotes \mathcal{E}^* corresponding to the dashed line in (b).

We consider a circularly polarized laser of vector potential $\mathbf{A}(t) = (\mathcal{E}/\Omega)[\cos(\Omega t)\hat{x} - \sin(\Omega t)\hat{y}]$ with electric field amplitude \mathcal{E} and angular-frequency Ω , which couples to electrons by minimal coupling $\mathbf{k} \rightarrow \mathbf{k} + e\mathbf{A}(t)/\hbar$, resulting in the time-periodic Hamiltonian $\hat{H}_0(t)$.

The periodic Hamiltonian $\hat{H}_0(t)$ gives rise to Floquet eigenstates $|\Phi_{\mathbf{k}\alpha}^{(\xi)}(t)\rangle$ with quasienergies $\varepsilon_{\mathbf{k}\alpha}^{(\xi)}$ satisfying $|\varepsilon_{\mathbf{k}\alpha}^{(\xi)}| < \frac{1}{2}\hbar\Omega$. We consider the regime $W \leq \hbar\Omega < 2W$ corresponding to a single photon resonance within the central TBG bands. Specifically, we consider $\Omega = 5$ meV/ \hbar and TBG at a near-magic twist angle of $\theta = 1.13^\circ$ whose Fermi velocity $v_F \approx 17$ km/s (corresponding to $W = 5$ meV in the Bistritzer-MacDonald model [29, 41]) is comparable to phonon speeds in TBG [42]. The drive mixes the two central bands $\nu = \pm 1$, resulting in quasienergies $\varepsilon_{\mathbf{k}\alpha}^{(\xi)}$, with upper and lower Floquet bands denoted by $\alpha = \pm$ (Fig. 2(d)) [24]. The drive

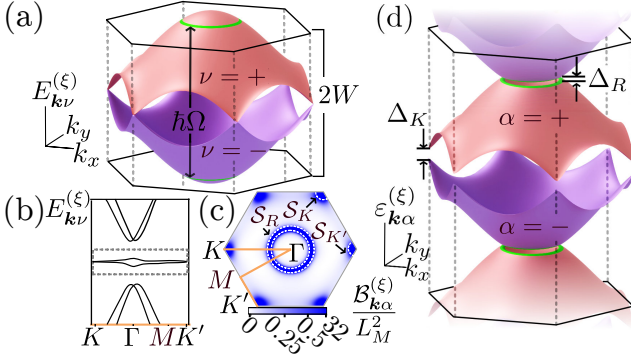


FIG. 2. (a) Schematic of flat bands in a moiré system used in numerical calculations. Drive with angular frequency Ω resonantly couples states along resonance rings (green). (b) Undriven spectrum of TBG along a line in the BZ (orange) demonstrated in (c). Dashed frame encloses optically-active central bands $\nu = \pm 1$. (c) Berry curvature $\mathcal{B}_{k\alpha}^{(\xi)}$ in the upper Floquet band, with blue color intensity proportional to $\tanh(2\mathcal{B}_{k+}^{(\xi)}/L_M^2)$ (color bar) so $\mathcal{B}_{k+}^{(\xi)}$ peaks are more visible. Dashed lines indicate areas enclosing $\mathcal{B}_{k+}^{(\xi)}$ peaks at the Dirac points and resonance ring. (d) Periodic quasienergy Floquet spectrum of the driven system, having two central bands shown in (a). The Floquet spectrum exhibits the upper (UFB, $\alpha = +$) and lower (LFB, $\alpha = -$) Floquet bands, separated by off-resonant gaps Δ_K at the Dirac K and K' points, and a Rabi-like gap Δ_R along the resonance ring [38–40].

opens off-resonant gaps of size $\Delta_K \approx 2e^2 v_F^2 \mathcal{E}^2 / \hbar \Omega^3$ at the Dirac points K and K' of the moiré Brillouin zone and a Rabi-like gap of $\Delta_R \sim V$ along the resonance ring, which is the ring on the \mathbf{k} -plane satisfying $E_{k+}^{(\xi)} - E_{k-}^{(\xi)} = \hbar \Omega$ (green rings in Fig. 2(a, d)). Here, v_F is the Fermi velocity of the undriven band structure, V is the energy scale of the drive, and the expression for Δ_K comes from the Van-Vleck perturbative expansion [33, 38, 40, 43–45].

The key components for stabilizing Floquet many-body states are electron interactions with low-temperature longitudinal TBG acoustic phonons:

$$\hat{H}_{\text{el-ph}} = \sum_{\mathbf{k}, \mathbf{q}, \mathbf{G}} M_{\mathbf{k}}^{\nu\nu'\xi}(\mathbf{q}, \mathbf{G}) \hat{c}_{\mathbf{k}+\mathbf{q}, \nu'}^{(\xi)\dagger} \hat{c}_{\mathbf{k}, \nu}^{(\xi)} (\hat{b}_{\mathbf{q}}^\dagger + \hat{b}_{-\mathbf{q}}) + \text{h.c.} \quad (1)$$

Here, \mathbf{G} is a moiré Brillouin zone reciprocal lattice vector, and $M_{\mathbf{k}}^{\nu\nu'\xi}(\mathbf{q}, \mathbf{G}) = D \sqrt{\hbar c_{\text{ph}} q} / (\sqrt{2} A_M \rho c_{\text{ph}}) \langle \xi \nu' \mathbf{k} + \mathbf{q} + \mathbf{G} | \xi \nu \mathbf{k} \rangle$ is the phonon-electron matrix element with deformation potential $D = 25$ eV, moiré unit cell area $A_M = \sqrt{3} L_M^2 / 2$, lattice vector length $L_M = a / [2 \sin(\theta/2)]$, monolayer graphene density ρ , and monolayer lattice vector length $a = 0.246$ nm. The operator $\hat{b}_{\mathbf{q}}$ creates an acoustic phonon mode of momentum \mathbf{q} with amplitude q , speed c_{ph} , and energy $\hbar c_{\text{ph}} q$. The speed of sound c_{ph} in TBG is roughly the same as that in monolayer graphene, but the small Brillouin zone in TBG folds the acoustic phonon dispersion into many branches [42]. The form-factor $\langle \xi \nu' \mathbf{k} + \mathbf{q} + \mathbf{G} | \xi \nu \mathbf{k} \rangle$ captures the decreasing coupling

of electrons to folded phonon branches with large \mathbf{G} [46]. We also include screened electronic interactions:

$$\hat{H}_{\text{el-el}} = \sum_{\mathbf{k}_1, \mathbf{k}_2, \mathbf{q}, \mathbf{G}} V_{\mathbf{k}_1, \mathbf{k}_2}^{\nu_1, \nu_2, \xi}(\mathbf{q}, \mathbf{G}) \hat{c}_{\mathbf{k}_1 + \mathbf{q}, \nu_1}^{(\xi)\dagger} \hat{c}_{\mathbf{k}_2 - \mathbf{q}, \nu_2}^{(\xi)\dagger} \hat{c}_{\mathbf{k}_1, \nu_1}^{(\xi)} \hat{c}_{\mathbf{k}_2, \nu_2}^{(\xi)}, \quad (2)$$

where $V_{\mathbf{k}_1, \mathbf{k}_2}^{\nu_1, \nu_2, \xi}(\mathbf{q}, \mathbf{G}) = V_b(\mathbf{q} + \mathbf{G})(1 - e^{-|\mathbf{q} + \mathbf{G}|d}) \langle \xi \nu_1 \mathbf{k}_1 + \mathbf{q} + \mathbf{G} | \xi \nu_1 \mathbf{k}_1 \rangle \langle \xi \nu_2 \mathbf{k}_2 - \mathbf{q} - \mathbf{G} | \xi \nu_2 \mathbf{k}_2 \rangle$ contains the screened Coulomb potential accounting for a dielectric of thickness $d = 13$ nm and dielectric constant ϵ separating a metallic gate from the TBG layers (Fig. 1(a)). Here, $V_g(\mathbf{q}) = e^2 / (2\pi \epsilon q A_M)$ is the bare Coulomb potential.

We focus on electron dynamics in its Floquet basis, treating interactions $\hat{H}_{\text{el-ph}}$ and $\hat{H}_{\text{el-el}}$ as weak perturbations scattering electrons between single-particle Floquet states [1–3, 34, 47]. The occupation probability $F_{\mathbf{k}\alpha}^{(\xi)}(t) = \langle \hat{f}_{\mathbf{k}\alpha}^{(\xi)\dagger}(t) \hat{f}_{\mathbf{k}\alpha}^{(\xi)}(t) \rangle$ is described by the Floquet-Boltzmann Equation (FBE) [3, 47],

$$\dot{F}_{\mathbf{k}\alpha}^{(\xi)}(t) = I_{\mathbf{k}\alpha}^{\text{el-ph}}[\{F_{\mathbf{k}\alpha}^{(\xi)}(t)\}] + I_{\mathbf{k}\alpha}^{\text{el-el}}[\{F_{\mathbf{k}\alpha}^{(\xi)}(t)\}]. \quad (3)$$

Here, $\hat{f}_{\mathbf{k}\alpha}^{(\xi)\dagger}(t)$ creates a single-particle electron state $|\Phi_{\mathbf{k}\alpha}^{(\xi)}(t)\rangle$, and $I_{\mathbf{k}\alpha}^{\text{el-ph}}$ and $I_{\mathbf{k}\alpha}^{\text{el-el}}$ are respectively the electron-phonon and electron-electron collision integrals, evaluated by the Fermi golden rule (see Supp. Mat. for FBE details [48]). The steady-state distribution yields $\dot{F}_{\mathbf{k}\alpha}^{(\xi)} = 0$, and the steady-state coherences between the Floquet states $\langle \hat{f}_{\mathbf{k}\alpha}^{(\xi)\dagger}(t) \hat{f}_{\mathbf{k}\alpha'}^{(\xi)}(t) \rangle$ for $\alpha \neq \alpha'$ are suppressed as long as $\tau_{\text{scat}}^{\text{el}}, \tau_{\text{scat}}^{\text{ph}} \gg \hbar / \Delta_R, \hbar / \Delta_K$, where $\tau_{\text{scat}}^{\text{el}}$ and $\tau_{\text{scat}}^{\text{ph}}$ are the electronic and electron-phonon scattering times, respectively [47, 49].

Transport properties.—To probe the electronic dynamics induced by the laser, we study the anomalous conductivity in the steady-state of the system [16, 31–35, 50–52]

$$\sigma_{xy} = \frac{2e^2}{h} \sum_{\alpha, \xi = \pm} \int \frac{d^2 \mathbf{k}}{(2\pi)^2} \mathcal{B}_{\mathbf{k}\alpha}^{(\xi)} F_{\mathbf{k}\alpha}^{(\xi)}, \quad (4)$$

which averages the product of Berry curvature [16, 40, 53]

$$\mathcal{B}_{\mathbf{k}\alpha}^{(\xi)} = \frac{\Omega}{\pi} \int_0^{2\pi/\Omega} dt \text{Im} \langle \partial_{k_x} \Phi_{\mathbf{k}\alpha}^{(\xi)}(t) | \partial_{k_y} \Phi_{\mathbf{k}\alpha}^{(\xi)}(t) \rangle, \quad (5)$$

and the steady-state fillings, $F_{\mathbf{k}\alpha}^{(\xi)}$. Without the drive, TBG has fragile topology with $\sigma_{xy} = 0$ at charge neutrality [54–56]. The circularly polarized laser breaks time-reversal symmetry between the valleys $\xi = \pm 1$, opens Haldane gaps in each valley, and produces nonzero σ_{xy} .

Our main finding is that σ_{xy} can be controlled by the field strength. It features a rapid drop as a function of the amplitude of the drive, \mathcal{E} , near the critical amplitude \mathcal{E}^* (Fig. 1(b)). This strong dependence on the external field indicates profound changes in the electronic steady-state distribution as the drive amplitude changes across

$\mathcal{E} = \mathcal{E}^*$. Furthermore, this strong amplitude-dependence arises only when the undriven effective electronic velocity v_{eff}^0 is close to c_{ph} in TBG (Fig. 1(c)), a condition unique to TBG near the “slow-electron” regime [36, 37]. Electrons in TBG are also decoupled from phonons in the dielectric medium, since typical screening media such as hBN have speeds of sound much larger than v_{eff}^0 [57].

Phenomenological analysis.—We explain the origin of the strong dependence of σ_{xy} on the drive amplitude near $\mathcal{E} = \mathcal{E}^*$ (Fig. 1(b)) by focusing on key processes affecting σ_{xy} , which involve momentum states (the K and K' points and resonance ring, see Fig. 2(c)) with large Berry curvature $\mathcal{B}_{\mathbf{k}\alpha}^{(\xi)}$. We assume that the steady-state occupation of the upper Floquet band (UFB, $\alpha = +$) and valley index ξ near K are uniform, $F_{\mathbf{k}+}^{(\xi)} = F_{K+}^{(\xi)}$, for $\mathbf{k} \in \mathcal{S}_K$, where \mathcal{S}_K is a small circle enclosing the full-width half maximum of the Berry curvature peak at K (Fig. 2(c)).

The steady-state occupation emerges as a balance between the total incoming and outgoing rate $\dot{F}_{K+}^{(\xi)}|_{\text{in}}, \dot{F}_{K+}^{(\xi)}|_{\text{out}}$, into \mathcal{S}_K from \mathcal{S}_{in} and into \mathcal{S}_{out} . Single phonon emission connecting the UFB \mathcal{S}_{in} with \mathcal{S}_K is the dominant contribution to $\dot{F}_{K+}^{(\xi)}|_{\text{in}}$. The two regions are connected by the phonon light-cone (Fig 3(a)). This rate is $\dot{F}_{K+}^{(\xi)}|_{\text{ph,in}} \approx \mathcal{R}_{\text{in}}(1 - F_{K+}^{(\xi)})F_{\text{in}}^{(\xi)}$, where $F_{\text{in}}^{(\xi)}$ is the average UFB occupation in \mathcal{S}_{in} , and \mathcal{R}_{in} is the average intrinsic scattering rate. Importantly, \mathcal{R}_{in} is proportional to the momentum-space area of \mathcal{S}_{in} , denoted \mathcal{A}_{in} , estimated by counting the UFB states that may scatter to \mathcal{S}_K by electron-phonon interactions. Hence, \mathcal{S}_{in} is the intersection between the UFB and phonon light-cones originating anywhere within \mathcal{S}_K (Fig. 3(a)). As Δ_R and Δ_K widen with \mathcal{E} , the Floquet bands become narrower [19, 24, 25], and \mathcal{A}_{in} shrinks, vanishing at $\mathcal{E} = \mathcal{E}^*$ (Fig. 3(b)). The critical strength \mathcal{E}^* is defined by $v_{\text{eff}}(\mathcal{E}^*) = c_{\text{ph}}$, where $v_{\text{eff}}(\mathcal{E}) = \max_{\mathbf{k}'}(\varepsilon_{\mathbf{k}'+}^{(\xi)} - \varepsilon_{\mathbf{K}+}^{(\xi)})/|\mathbf{k}' - \mathbf{K}|$ is the electronic velocity near the K point. By estimating $v_{\text{eff}}(\mathcal{E})$, one finds that $\mathcal{E}^* \propto [1 - c_{\text{ph}}/v_{\text{eff}}^0]^\gamma$ for small $1 - c_{\text{ph}}/v_{\text{eff}}^0$, where γ depends on the quasienergy structure and $v_{\text{eff}}^0 \equiv v_{\text{eff}}(0)$. One can also show $\mathcal{A}_{\text{in}} \propto \max(\mathcal{E} - \mathcal{E}^*, 0)$ as $\mathcal{E} \rightarrow \mathcal{E}^*$. (See Supp. Mat. [48].)

Similarly, the phonon-mediated outgoing rate is $\dot{F}_{K+}^{(\xi)}|_{\text{ph,out}} \approx \mathcal{R}_{\text{out}}F_{K+}^{(\xi)}(1 - F_{\text{out}}^{(\xi)})$, where $F_{\text{out}}^{(\xi)}$ is the lower Floquet band (LFB, $\alpha = -$) average occupation in \mathcal{S}_{out} , and \mathcal{R}_{out} is the average intrinsic rate, proportional to $\mathcal{A}_{\text{out}} = \int_{\mathcal{S}_{\text{out}}} d^2\mathbf{k}$, where \mathcal{S}_{out} is the momentum region enclosing intersections between the LFB with phonon light cones originating from states in \mathcal{S}_K (Fig. 3(a)). However, unlike \mathcal{A}_{in} , \mathcal{A}_{out} does not vanish as $\mathcal{E} \rightarrow \mathcal{E}^*$ and instead expands as \mathcal{E} increases.

Electronic interactions and photon-mediated Floquet-Umklapp (FU) processes introduce additional terms in the rate equation depending smoothly on \mathcal{E} and roughly uniformly-spread in momentum. We thus add an incoming rate $\dot{F}_{K+}^{(\xi)}|_{\text{r,in}} = \Gamma_{\text{in}}(1 - F_{K+}^{(\xi)})$ and outgoing rate

$\dot{F}_{K+}^{(\xi)}|_{\text{r,out}} = \Gamma_{\text{out}}F_{K+}^{(\xi)}$ with constant Γ_{in} and Γ_{out} to the rate equations. The strength of FU processes is weaker than \mathcal{R}_{in} and \mathcal{R}_{out} by factors of roughly $(v_F e\mathcal{E}/\Omega^2)^{2n}$, where $|n| > 1$ is the number of photons emitted or absorbed [3]. The processes also impart large phonon momentum transfers which the form-factor in Eq. 1 suppresses.

The total rate equation is:

$$\dot{F}_{K+}^{(\xi)} = \dot{F}_{K+}^{(\xi)}|_{\text{ph,in}} - \dot{F}_{K+}^{(\xi)}|_{\text{ph,out}} + \dot{F}_{K+}^{(\xi)}|_{\text{r,in}} - \dot{F}_{K+}^{(\xi)}|_{\text{r,out}}. \quad (6)$$

At the steady-state, $\dot{F}_{K+}^{(\xi)} = 0$, so

$$F_{K+}^{(\xi)} = \frac{\mathcal{R}_{\text{in}}F_{\text{in}}^{(\xi)} + \Gamma_{\text{in}}}{\mathcal{R}_{\text{in}}F_{\text{in}}^{(\xi)} + \mathcal{R}_{\text{out}} + \Gamma_{\text{in}} + \Gamma_{\text{out}}}. \quad (7)$$

Since $\mathcal{R}_{\text{in}} \propto \mathcal{A}_{\text{in}}$, it decreases as a function of \mathcal{E} and eventually shrinks to zero for $\mathcal{E} \geq \mathcal{E}^*$ (see Fig. 3(b) for numerical verification). We expect a similar \mathcal{E} -dependence of $F_{K-}^{(\xi)}$ and σ_{xy} , yet smeared by additional scattering rates appearing in Eq. 7, as demonstrated numerically in Fig. 1(b).

Scattering rates about K' and K points, related by a $\pi/3$ rotation, contribute equally to σ_{xy} . The resonance ring vicinity, \mathcal{S}_R (Fig. 2(c)), yields a similar \mathcal{E} -dependence, with a much lower critical field \mathcal{E}_R^* due to different effective electronic velocities near the resonance ring. Indeed, in Figs. 1(b) and 3(b), \mathcal{E}_R^* is not visible for the drive strengths plotted. Finally, we find the contribution of the LFB to σ_{xy} using particle-hole symmetry, $F_{K-}^{(\xi)} = 1 - F_{K+}^{(\xi)}$ and $\mathcal{B}_{K-}^{(\xi)} = -\mathcal{B}_{K+}^{(\xi)}$. Thus, we can reproduce qualitatively the numerical result (Fig. 3) of the suppression of σ_{xy} with \mathcal{E} .

Numerical analysis.—The results in Fig. 3(b-d) utilized a simplified toy model describing TBG as a tight-binding hexagonal lattice, similar to graphene [58], but with parameters tuned to match v_F and the Brillouin zone size of TBG. This model misses some subtle details, but captures the interplay between electron and phonon velocities and the large Berry curvature at the Dirac points and resonance ring. The model represents only the central $\nu = \pm 1$ bands of the undriven band-structure, but since the low drive angular frequency Ω is only resonant to these flat bands, we can ignore the $|\nu| > 1$ bands. This is valid only when θ is near the magic angle where the $|\nu| > 1$ and $\nu = \pm 1$ bands are well-separated. In the Supp. Mat. [48], we present the numerical analysis of a continuum model without electronic interactions [29, 41, 59], which yields qualitatively similar results. In the toy model, $v_{\text{eff}}^0 = 18.9$ km/s, and we select $c_{\text{ph}} \in [17.9 \text{ km/s}, 19.4 \text{ km/s}]$ (see Fig. 1). In the range $c_{\text{ph}} < v_{\text{eff}}^0$, the drive induces the regime $c_{\text{ph}} > v_{\text{eff}}(\mathcal{E})$ for $\mathcal{E} > \mathcal{E}^*$. Calculating $\langle \xi\nu\mathbf{k} + \mathbf{q} + \mathbf{G} | \xi\nu\mathbf{k} \rangle$ relies on the continuum model [46, 48], and needs to be introduced by hand in the toy model, so we approximate $\langle \xi\nu\mathbf{k} + \mathbf{q} | \xi\nu\mathbf{k} \rangle \approx \delta_{\nu,\nu'} e^{-l_w^2 q^2/4}$, with $l_w \approx L_M/(5\sqrt{3})$

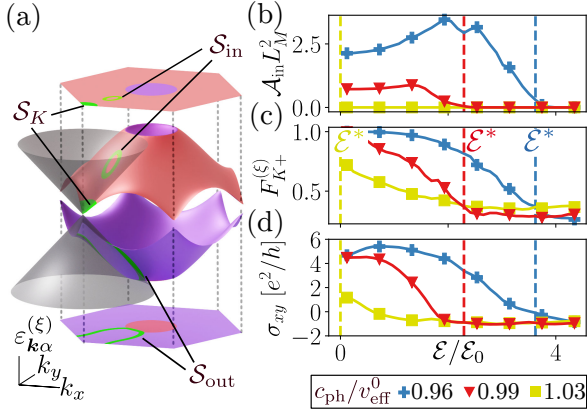


FIG. 3. (a) Schematics of the Floquet spectrum and one of the phonon light-cones originating from the area S_K in the UFB. The intersection between the UFB (LFB) and all cones centered in S_K form S_{in} (S_{out}). As $\mathcal{E} \rightarrow \mathcal{E}^*$, the area of S_{in} vanishes. (b-d) Numerical verification of the phenomenological model. (b) Area of S_{in} , \mathcal{A}_{in} , vs. \mathcal{E} for three values of c_{ph}/v_{eff}^0 . (c) Average occupation of states in S_K . (d) Anomalous Hall conductivity σ_{xy} for the same parameters as (b, c). At \mathcal{E}^* (dashed lines), \mathcal{A}_{in} , $F_{K+}^{(\mathcal{E})}$, and σ_{xy} plateau.

representing the spatial extent of the Wannier orbitals localized to TBG layer alignment sites [46].

First, we show how solving the FBE (Eq. 3) for the steady-state distribution verifies the phenomenological model. Consider the non-interacting limit by solving Eq. 3 for $F_{\mathbf{k}\alpha}^{(\mathcal{E})}$ with $\epsilon \rightarrow \infty$ ($I_{\mathbf{k}\alpha}^{el-el} = 0$). The left two quadrants of Fig. 4(a) show the non-interacting steady-state distributions for a low phonon bath temperature of 1 K and $c_{ph} = 0.98v_{eff}^0$ in the $\mathcal{E} > \mathcal{E}^*$ and $\mathcal{E} < \mathcal{E}^*$ cases. In the $\mathcal{E} > \mathcal{E}^*$ case (left top quadrant), the K, K' points (blue) have a reduced occupation relative to the $\mathcal{E} < \mathcal{E}^*$ case (left bottom quadrant), due to the suppression of the incoming scattering rates into $S_{K,K'}$ (verifying the phenomenological model). Fig. 3(c) shows the occupation near the K point, $F_{K+}^{(\mathcal{E})}$, as a function of \mathcal{E} for three values of c_{ph}/v_{eff}^0 and verifies \mathcal{A}_{in} , $F_{K+}^{(\mathcal{E})}$, and σ_{xy} plateau at the same critical $\mathcal{E} = \mathcal{E}^*$.

Next, we quantify the strength of Coulomb screening necessary to stabilize the steady-state. We include $I_{\mathbf{k}\alpha}^{el-el} \neq 0$, using finite ϵ . On the right top and bottom quadrants of Fig. 4(a), we show the resulting steady-state occupations, which have higher entropy than the non-interacting case. Strong drive strengths result in enhanced electron-electron FU processes, heating the system to nearly uniformly-filled Floquet bands (right top quadrant), resulting in $\sigma_{xy} \approx 0$ in the regime $\mathcal{E} > \mathcal{E}^*$ (Fig. 1(b)). The entropy of the steady-state occupation depends on the balance between electron-phonon cooling processes and electron-electron heating processes and is therefore sensitive to ϵ and gate distance d . Fig. 1(b) shows the steady-state conductivity as a function of \mathcal{E}

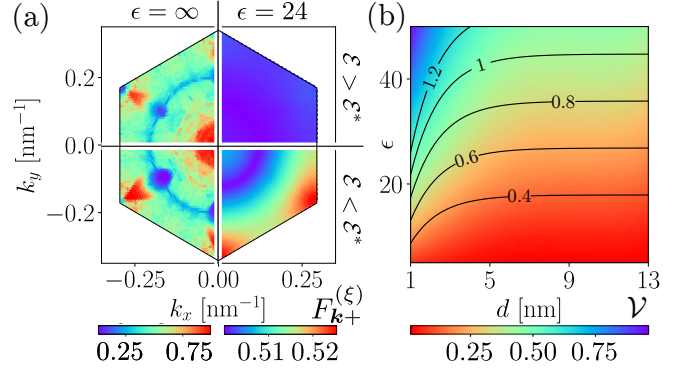


FIG. 4. (a) Left column: steady-state occupation of the UFB in when $\epsilon = \infty$. Right column: steady-state occupation for same parameters, but $\epsilon = 24$. Top row: $\mathcal{E}/\mathcal{E}_0 = 3.14 > \mathcal{E}^*/\mathcal{E}_0$ case where the population at K is depleted. Bottom row: $\mathcal{E}/\mathcal{E}_0 = 2.17 < \mathcal{E}^*/\mathcal{E}_0$ case. (b) Visibility \mathcal{V} vs. ϵ and gate distance d . Blue region: regime where electron-phonon interactions dominate. Contours: points with fixed ratio of electron-phonon V_{ph} to electron-electron V_{el} characteristic interaction strengths; numbers on contours give the value of V_{ph}/V_{el} (see text for definition).

for various ϵ , with deformation potential $D = 25$ eV and $d = 13$ nm. The slope $\partial_{\mathcal{E}}\sigma_{xy}$ in the $\mathcal{E} < \mathcal{E}^*$ regime where σ_{xy} is less steep as ϵ decreases. To quantify this, we define a visibility parameter $\mathcal{V} = -\overline{\partial_{\mathcal{E}}\sigma_{xy}}/[(e^2/h)/\mathcal{E}_0]$ where $\overline{\partial_{\mathcal{E}}\sigma_{xy}}$ denotes an average of $\partial_{\mathcal{E}}\sigma_{xy}$ across a window $\mathcal{E}^* - \delta\mathcal{E} < \mathcal{E} < \mathcal{E}^*$ where $\delta\mathcal{E}/\mathcal{E}_0 = 1.45$ denotes a range of amplitudes in which σ_{xy} decreases rapidly (shaded region in Fig. 1(b)). In Fig. 4(b), we show \mathcal{V} as a function of d and ϵ , keeping $D = 25$ eV and $\delta\mathcal{E}$ constant. In the red region (small ϵ , d) electron-electron interactions dominate, and the system reaches a hot steady-state with low visibility; in the blue region, phonon cooling dominates and a low-entropy steady-state appears. The contours compare the electron-phonon energy scale $V_{ph} \approx D\sqrt{\hbar c_{ph}}|\mathbf{K}|/(\sqrt{2A_M\rho c_{ph}})e^{-|\mathbf{K}|^2 t_w^2/4}$ to the electron-electron energy scale $V_{el} \approx e^2/(2\pi\epsilon A_M|\mathbf{K}|)(1 - e^{-2|\mathbf{K}|d})e^{-|\mathbf{K}|^2 t_w^2/2}$ (Eqs. 1 and 2), evaluated for a characteristic momentum transfer $|\mathbf{K}| = 4\pi/(3L_M)$ we choose to be that of the K point.

Conclusion—TBG is a remarkable system where the Fermi velocity is comparable to the speed of sound. Upon THz-laser driving, the electronic population dynamics exhibits bottlenecks for electron-phonon scattering into high-Berry curvature Floquet states, strongly affecting the anomalous Hall transport. These bottlenecks can be sensitively controlled by the drive amplitude. If the undriven effective electron speed is faster than sound $v_{eff}^0 > c_{ph}$, a drive with $\mathcal{E} > \mathcal{E}^*$ induces the opposite regime $v_{eff}(\mathcal{E}) < c_{ph}$, decouples the electrons from the phonons, and suppresses the Hall conductivity (Fig. 1(b)). We also find that a strong drive field-dependence of σ_{xy} arises for efficient Coulomb screening, e.g., by a close-by gate or a strong dielectric [60–62]. Experiment-

tal advances in Floquet engineering [32], and THz laser sources [63], show that our predictions should be accessible experimentally.

Theoretical analysis of UV-visible or X-ray driven TBG are a subject of future work, which must account for dispersive bands that mix significantly with the flat bands [24, 28]. High-frequency drives could further reduce heating, facilitating fewer electron-electron FU processes [3] while making use of enhanced electron-phonon Umklapp cooling processes arising from tightly-localized Wannier orbitals in TBG [46]. (In the resonant frequency limit considered in this work, momentum electron-phonon Umklapp processes are simultaneously suppressed Floquet-Umklapp processes.) Another interesting direction involves symmetry broken phases in the steady-state of strongly coupled TBG [2]. We leave these exciting directions to future studies.

We thank Netanel Lindner, Mark Rudner, Or Katz, Gaurav Gupta, Seamus O'Hara, Jason Alicea, Alex Thomson, Felix von Oppen and Kryštof Kolář for valuable discussions. C.Y. gratefully acknowledges support from the DOE NNSA Stewardship Science Graduate Fellowship program, which is provided under cooperative agreement number DE-NA0003960. C.L. acknowledges support by the Gordon and Betty Moore Foundation's EPiQS Initiative, Grant GBMF8682, start-up funds from Florida State University and the National High Magnetic Field Laboratory. The National High Magnetic Field Laboratory is supported by the National Science Foundation through NSF/DMR-1644779 and the state of Florida. G.R. and I.E. are grateful for support from the Simons Foundation and the Institute of Quantum Information and Matter, as well as support from the NSF DMR grant number 1839271. This work is supported by ARO MURI Grant No. W911NF-16-1-0361, and was performed in part at Aspen Center for Physics, which is supported by National Science Foundation grant PHY-1607611.

-
- [1] I. Esin, M. S. Rudner, and N. H. Lindner, *Science Advances* **6**, eaay4922 (2020).
 - [2] I. Esin, G. Gupta, E. Berg, M. Rudner, and N. Lindner, *Nature Communications* **12** (2021), 10.1038/s41467-021-25511-9.
 - [3] K. I. Seetharam, C.-E. Bardyn, N. H. Lindner, M. S. Rudner, and G. Refael, *Phys. Rev. B* **99**, 014307 (2019).
 - [4] A. Castro, U. De Giovannini, S. A. Sato, H. Hübener, and A. Rubio, *Phys. Rev. Res.* **4**, 033213 (2022).
 - [5] D. Fausti, R. I. Tobey, N. Dean, S. Kaiser, A. Dienst, M. C. Hoffmann, S. Pyon, T. Takayama, H. Takagi, and A. Cavalleri, *Science* **331**, 189 (2011).
 - [6] N. Fläschner, B. S. Rem, M. Tarnowski, D. Vogel, D.-S. Lühmann, K. Sengstock, and C. Weitenberg, *Science* **352**, 1091 (2016).
 - [7] M. Nuske, L. Broers, B. Schulte, G. Jotzu, S. A. Sato, A. Cavalleri, A. Rubio, J. W. McIver, and L. Mathey, *Phys. Rev. Res.* **2**, 043408 (2020).
 - [8] S. Fazzini, P. Chudzinski, C. Daur, I. Schneider, and S. Eggert, *Phys. Rev. Lett.* **126**, 243401 (2021).
 - [9] N. H. Lindner, G. Refael, and V. Galitski, *Nat. Phys.* **7**, 490 (2011).
 - [10] M. Vogl, S. Chaudhary, and G. A. Fiete, *Journal of Physics: Condensed Matter* **35**, 095801 (2022).
 - [11] I. A. Assi, J. P. F. LeBlanc, M. Rodriguez-Vega, H. Bahlouli, and M. Vogl, *Phys. Rev. B* **104**, 195429 (2021).
 - [12] M. Rodriguez-Vega, M. Vogl, and G. A. Fiete, *Phys. Rev. Res.* **2**, 033494 (2020).
 - [13] M. Vogl, M. Rodriguez-Vega, B. Flebus, A. H. MacDonald, and G. A. Fiete, *Phys. Rev. B* **103**, 014310 (2021).
 - [14] M. Liu, H. Y. Hwang, H. Tao, A. C. Strikwerda, K. Fan, G. R. Keiser, A. J. Sternbach, K. G. West, S. Kittiwatanakul, J. Lu, S. A. Wolf, F. G. Omenetto, X. Zhang, K. A. Nelson, and R. D. Averitt, *Nature* **487**, 345 (2012).
 - [15] A. X. Gray, M. C. Hoffmann, J. Jeong, N. P. Aetukuri, D. Zhu, H. Y. Hwang, N. C. Brandt, H. Wen, A. J. Sternbach, S. Bonetti, A. H. Reid, R. Kukreja, C. Graves, T. Wang, P. Granitzka, Z. Chen, D. J. Higley, T. Chase, E. Jal, E. Abreu, M. K. Liu, T.-C. Weng, D. Sokaras, D. Nordlund, M. Chollet, R. Alonso-Mori, H. Lemke, J. M. Glowia, M. Trigo, Y. Zhu, H. Ohldag, J. W. Freeland, M. G. Samant, J. Berakdar, R. D. Averitt, K. A. Nelson, S. S. P. Parkin, and H. A. Dürr, *Phys. Rev. B* **98**, 045104 (2018).
 - [16] I. Esin, M. S. Rudner, G. Refael, and N. H. Lindner, *Phys. Rev. B* **97**, 245401 (2018).
 - [17] A. Kumar, M. Rodriguez-Vega, T. Pereg-Barnea, and B. Seradjeh, *Phys. Rev. B* **101**, 174314 (2020).
 - [18] H. Chono, K. Takasan, and Y. Yanase, *Phys. Rev. B* **102**, 174508 (2020).
 - [19] H. Dehghani, M. Hafezi, and P. Ghaemi, *Phys. Rev. Res.* **3**, 023039(R) (2021).
 - [20] J. Shan, M. Ye, H. Chu, S. Lee, J.-G. Park, L. Balents, and D. Hsieh, *Nature* **600**, 235 (2021).
 - [21] E. L. Wong, A. J. Winchester, V. Pareek, J. Madéo, M. K. L. Man, and K. M. Dani, *Science Advances* **4**, eaat9722 (2018).
 - [22] T. Kitagawa, T. Oka, A. Brataas, L. Fu, and E. Demler, *Phys. Rev. B* **84**, 235108 (2011).
 - [23] M. H. Michael, M. Först, D. Nicoletti, S. R. U. Haque, Y. Zhang, A. Cavalleri, R. D. Averitt, D. Podolsky, and E. Demler, *Phys. Rev. B* **105**, 174301 (2022).
 - [24] O. Katz, G. Refael, and N. H. Lindner, *Phys. Rev. B* **102**, 155123 (2020).
 - [25] Y. Li, H. A. Fertig, and B. Seradjeh, *Phys. Rev. Res.* **2**, 043275 (2020).
 - [26] G. E. Topp, G. Jotzu, J. W. McIver, L. Xian, A. Rubio, and M. A. Sentef, *Phys. Rev. Res.* **1**, 023031 (2019).
 - [27] M. Vogl, M. Rodriguez-Vega, and G. A. Fiete, *Phys. Rev. B* **101**, 241408(R) (2020).
 - [28] M. Vogl, M. Rodriguez-Vega, and G. A. Fiete, *Phys. Rev. B* **101**, 235411 (2020).
 - [29] R. Bistritzer and A. MacDonald, *Proceedings of the National Academy of Sciences of the United States of America* **108** (2010), 10.1073/pnas.1108174108.
 - [30] H. Dehghani, T. Oka, and A. Mitra, *Phys. Rev. B* **90**, 195429 (2014).
 - [31] H. Dehghani, T. Oka, and A. Mitra, *Phys. Rev. B* **91**, 155422 (2015).

- [32] J. McIver, B. Schulte, F.-U. Stein, T. Matsuyama, G. Jotzu, G. Meier, and A. Cavalleri, *Nature Physics* **16**, 1 (2020).
- [33] T. Oka and H. Aoki, *Phys. Rev. B* **79**, 081406(R) (2009).
- [34] S. A. Sato, J. W. McIver, M. Nuske, P. Tang, G. Jotzu, B. Schulte, H. Hübener, U. De Giovannini, L. Mathey, M. A. Sentef, A. Cavalleri, and A. Rubio, *Phys. Rev. B* **99**, 214302 (2019).
- [35] S. A. Sato, P. Tang, M. A. Sentef, U. D. Giovannini, H. Hübener, and A. Rubio, *New Journal of Physics* **21**, 093005 (2019).
- [36] I. Esin, I. Esterlis, E. Demler, and G. Refael, “Generating coherent phonon waves in narrow-band materials: a twisted bilayer graphene phaser,” (2022), [arXiv:2207.11245 \[cond-mat\]](https://arxiv.org/abs/2207.11245).
- [37] G. Sharma, I. Yudhistira, N. Chakraborty, D. Ho, M. Al Ezzi, M. Fuhrer, G. Vignale, and S. Adam, *Nature Communications* **12** (2021), 10.1038/s41467-021-25864-1.
- [38] O. Karni, I. Esin, and K. M. Dani, *Advanced Materials* **n/a**, 2204120.
- [39] M. Rodriguez-Vega, M. Vogl, and G. Fiete, *Annals of Physics* **435**, 168434 (2021).
- [40] M. Rudner and N. Lindner, *Nature Reviews Physics* **2**, 1 (2020).
- [41] M. Koshino, N. F. Q. Yuan, T. Koretsune, M. Ochi, K. Kuroki, and L. Fu, *Phys. Rev. X* **8**, 031087 (2018).
- [42] M. Koshino and Y.-W. Son, *Phys. Rev. B* **100**, 075416 (2019).
- [43] G. Usaj, P. M. Perez-Piskunow, L. E. F. Foa Torres, and C. A. Balseiro, *Phys. Rev. B* **90**, 115423 (2014).
- [44] S. Aeschlimann, S. A. Sato, R. Krause, M. Chávez-Cervantes, U. De Giovannini, H. Hübener, S. Forti, C. Coletti, K. Hanff, K. Rosnagel, A. Rubio, and I. Gierz, *Nano Letters* **21**, 5028 (2021), pMID: 34082532, <https://doi.org/10.1021/acs.nanolett.1c00801>.
- [45] M. S. Rudner and N. H. Lindner, “The floquet engineer’s handbook,” (2020), [arXiv:2003.08252 \[cond-mat\]](https://arxiv.org/abs/2003.08252).
- [46] H. Ishizuka, A. Fahimniya, F. Guinea, and L. Levitov, *Nano Letters* **21**, 7465 (2021), pMID: 34515488, <https://doi.org/10.1021/acs.nanolett.1c00565>.
- [47] K. I. Seetharam, C.-E. Bardyn, N. H. Lindner, M. S. Rudner, and G. Refael, *Phys. Rev. X* **5**, 041050 (2015).
- [48] [URL_will_be_inserted_by_publisher.](#)
- [49] W. Kohn, *Journal of Statistical Physics* **103**, 417 (2001).
- [50] A. Chandran and S. L. Sondhi, *Phys. Rev. B* **93**, 174305 (2016).
- [51] A. Tomadin, S. Diehl, and P. Zoller, *Phys. Rev. A* **83**, 013611 (2011).
- [52] H. Dehghani and A. Mitra, *Phys. Rev. B* **93**, 245416 (2016).
- [53] T. Fukui, Y. Hatsugai, and H. Suzuki, *Journal of the Physical Society of Japan* **74**, 1674 (2005), <https://doi.org/10.1143/JPSJ.74.1674>.
- [54] K. Nuckolls, M. Oh, D. Wong, B. Lian, K. Watanabe, T. Taniguchi, B. Bernevig, and A. Yazdani, *Nature* **588**, 1 (2020).
- [55] C. Repellin and T. Senthil, *Phys. Rev. Res.* **2**, 023238 (2020).
- [56] Y. Xie, A. Pierce, J. Park, D. Parker, E. Khalaf, P. Ledwith, Y. Cao, S. Lee, S. Chen, P. Forrester, K. Watanabe, T. Taniguchi, A. Vishwanath, P. Jarillo-Herrero, and A. Yacoby, *Nature* **600**, 439 (2021).
- [57] J. D. G. Greener, A. V. Akimov, V. E. Gusev, Z. R. Kudrynskiy, P. H. Beton, Z. D. Kovalyuk, T. Taniguchi, K. Watanabe, A. J. Kent, and A. Patanè, *Phys. Rev. B* **98**, 075408 (2018).
- [58] Q. Chen, L. Du, and G. A. Fiete, *Phys. Rev. B* **97**, 035422 (2018).
- [59] H. J. Monkhorst and J. D. Pack, *Phys. Rev. B* **13**, 5188 (1976).
- [60] A. Coissard, D. Wander, H. Vignaud, A. G. Grushin, C. Repellin, K. Watanabe, T. Taniguchi, F. Gay, C. B. Winkelmann, H. Courtois, H. Sellier, and B. Sacépé, *Nature* **605**, 51 (2022).
- [61] L. Veyrat, D. Corentin, A. Coissard, X. Li, F. Gay, K. Watanabe, T. Taniguchi, Z. Han, B. Piot, H. Sellier, and B. Sacépé, *Science* **367**, 781 (2020).
- [62] T. Sakudo and H. Unoki, *Phys. Rev. Lett.* **26**, 851 (1971).
- [63] R. A. Lewis, *Journal of Physics D: Applied Physics* **47**, 374001 (2014).

Supplemental Material: Optical Control of Slow Topological Electrons in Moiré Systems

Christopher Yang, Iliya Esin, Cyprian Lewandowski, and Gil Refael

I. DETAILS OF THE MODELS

In both the toy and continuum models, we take the undriven Hamiltonians $H(\mathbf{k})$ and obtain the time-dependent Hamiltonian $H(\mathbf{k}, t)$ via minimal coupling $\mathbf{k} \rightarrow \mathbf{k} + e\mathbf{A}(t)/\hbar$. Here,

$$\mathbf{A}(t) = A[\cos(\Omega t)\hat{\mathbf{x}} - \sin(\Omega t)\hat{\mathbf{y}}] \quad (\text{S1})$$

is the magnetic vector potential of circularly polarized laser. We can expand the time-dependent eigenstates of the Hamiltonian in a Floquet-Bloch basis [1]:

$$|\psi_{\mathbf{k}\alpha}(t)\rangle = e^{-i\varepsilon_{\alpha}^{(\xi)}t/\hbar}|\Phi_{\mathbf{k}\alpha}^m(t)\rangle, \quad (\text{S2})$$

where \mathbf{r} is the position vector, $|\Phi_{\mathbf{k}\alpha}^m(t)\rangle$ is periodic in time ($|\Phi_{\mathbf{k}\alpha}^m(t)\rangle = |\Phi_{\mathbf{k}\alpha}^m(t+2\pi/\Omega)\rangle$), $\varepsilon_{\alpha}^{(\xi)}$ are the quasienergies plotted in Fig. 2(d), and α enumerates the Floquet quasienergy bands. To determine the Floquet-Bloch basis, it is easiest to expand the time-dependent $|\Phi_{\mathbf{k}\alpha}^m(t)\rangle$ in terms of time-independent Fourier harmonics $|\phi_{\mathbf{k}\alpha}^m\rangle$,

$$|\Phi_{\mathbf{k}\alpha}^m(t)\rangle = \sum_m e^{-im\Omega t}|\phi_{\mathbf{k}\alpha}^m\rangle, \quad (\text{S3})$$

take a Fourier transform the Hamiltonian,

$$H(\mathbf{k}, t) = \sum_m e^{-im\Omega t} H^{(m)}(\mathbf{k}), \quad (\text{S4})$$

and solve the Schrödinger equation in the basis of Floquet harmonics:

$$(\varepsilon_{\alpha}^{(\xi)} + m\hbar\Omega)|\phi_{\mathbf{k}\alpha}^m\rangle = \sum_{m'} H^{(m-m')}(\mathbf{k})|\phi_{\mathbf{k}\alpha}^{m'}\rangle. \quad (\text{S5})$$

In the following subsections, we detail the exact form of the Floquet Hamiltonians.

A. Tight binding Floquet toy Hamiltonian

We use a rescaled, two-band tight binding model for graphene to replicate the flat conduction and valence bands of TBG. In the rescaled Hamiltonian

$$H_{\text{toy}}(\mathbf{k}) = \begin{pmatrix} 0 & h_{\mathbf{k}} \\ h_{\mathbf{k}}^* & 0 \end{pmatrix}, \quad (\text{S6})$$

$$h_{\mathbf{k}} = \frac{W}{3} \sum_j e^{i\mathbf{k}\cdot\boldsymbol{\delta}_j}, \quad (\text{S7})$$

we choose long hopping vectors

$$\boldsymbol{\delta}_j = L_M/\sqrt{3}[\sin(2\pi m/3)\hat{\mathbf{x}} + \cos(2\pi m/3)\hat{\mathbf{y}}], \quad (\text{S8})$$

with $L_M = 0.246 \text{ nm}/(2\sin\theta/2)$, and a narrow bandwidth W . The corresponding rescaled eigenenergies and Bloch states are

$$E_{\nu}(\mathbf{k}) = \nu|h_{\mathbf{k}}|, \quad (\text{S9})$$

and

$$|\nu\mathbf{k}\rangle = \frac{1}{\sqrt{2}} \begin{pmatrix} \nu e^{i\arg(h_{\mathbf{k}})} \\ 1 \end{pmatrix}, \quad (\text{S10})$$

respectively, with $\nu = \pm 1$ enumerating the flat Bloch bands.

Following [2], we perform minimal coupling, which turns the functions $h_{\mathbf{k}}$ into time-dependent quantities with Fourier transforms

$$\begin{aligned} h_{\mathbf{k}}^{(n)} &= \frac{1}{2\pi/\Omega} \int_0^{2\pi/\Omega} h_{\mathbf{k}+e\mathbf{A}(t)/\hbar} e^{-in\Omega t} dt \\ &= \sum_j t e^{i\mathbf{k}\cdot\boldsymbol{\delta}_j} e^{in\phi_j} J_n(-\tilde{\mathcal{E}}), \end{aligned} \quad (\text{S11})$$

where $\tilde{\mathcal{E}}$ is the dimensionless drive strength

$$\tilde{\mathcal{E}} = \frac{eL_M}{\sqrt{3}\hbar} A = \frac{eL_M}{\sqrt{3}\hbar} \frac{\mathcal{E}}{\Omega}; \quad (\text{S12})$$

the phase angles are $\phi_0 = \pi/2$, $\phi_1 = -5\pi/6$, and $\phi_2 = -\pi/6$; and

$$J_n(z) = \frac{1}{2\pi i^n} \int_0^{2\pi} e^{iz\cos\theta} e^{in\theta} d\theta. \quad (\text{S13})$$

The Fourier-transformed Hamiltonian is

$$H_{\text{toy}}^{(n)}(\mathbf{k}) = \begin{pmatrix} 0 & h_{\mathbf{k}}^{(n)} \\ h_{\mathbf{k}}^{*(n)} & 0 \end{pmatrix}. \quad (\text{S14})$$

Note that

$$h_{\mathbf{k}}^{*(n)} = \sum_j t e^{-i\mathbf{k}\cdot\boldsymbol{\delta}_j} e^{in\phi_j} J_n(\tilde{\mathcal{E}}) \quad (\text{S15})$$

is the Fourier transform of the conjugate of $h_{\mathbf{k}}$. In simulations, we generally truncate the Fourier Hamiltonian (Eq. S5) to $-12 \leq m \leq 12$, so that we account for a sufficient number of high-order Floquet-Umklapp processes in the Floquet-Boltzmann equation. For both the undriven and Floquet Hamiltonians, we also perform a gauge transformation, replacing $h_{\mathbf{k}}^{(n)} \rightarrow i e^{-i\mathbf{k}\cdot\boldsymbol{\delta}_0} h_{\mathbf{k}}^{(n)}$ and $h_{\mathbf{k}} \rightarrow -i e^{i\mathbf{k}\cdot\boldsymbol{\delta}_0} h_{\mathbf{k}}$ to make the Hamiltonians periodic by shifts of $\mathbf{k} \rightarrow \mathbf{k} + \mathbf{G}$, where \mathbf{G} is a reciprocal lattice vector.

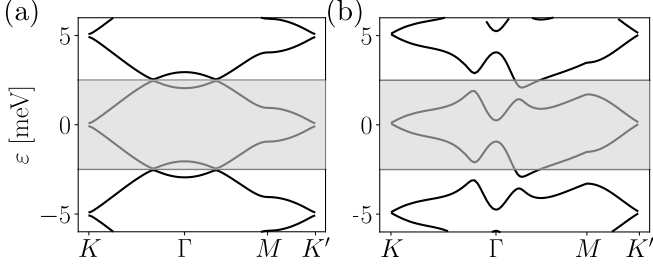


FIG. S1. (a) The quasienergy band structure of the toy model with for the parameters used in the main text. (b) The quasienergy band structure of the continuum model at valley $\xi = +1$. In both panels, the first Floquet Brillouin zone is shaded. See Sec. II for details and justification for the parameters we have used.

B. Continuum Model Floquet Hamiltonian

The undriven continuum model for TBG [3] describes the bandstructure of TBG near the valley $\xi = \pm 1$ of the monolayer graphene Brillouin zone. Its Hamiltonian

$$H_\xi = \begin{pmatrix} H_1 & U^\dagger \\ U & H_2 \end{pmatrix} \quad (\text{S16})$$

is diagonalized in the basis $\psi_{n\mathbf{k}} = (\psi_{n\mathbf{k}}^{A_1}, \psi_{n\mathbf{k}}^{B_1}, \psi_{n\mathbf{k}}^{A_2}, \psi_{n\mathbf{k}}^{B_2})^T$ with

$$\psi_{n\mathbf{k}}^X(\mathbf{r}) = e^{i\mathbf{k}\cdot\mathbf{r}} \sum_{\mathbf{G}} C_{n\mathbf{k}}^X(\mathbf{G}) e^{i\mathbf{G}\cdot\mathbf{r}} \quad (\text{S17})$$

where $X = A_l, B_l$ represents sublattice A or B degree of freedom in layer index $l = \pm 1$. In Eq. S16, H_l are the monolayer graphene Hamiltonians, which, in close vicinity of the $\xi = \pm 1$ valleys, resemble Dirac cones:

$$H_l = -\hbar v_F^{\text{ml}} \left[R(l\theta/2)(\mathbf{k} - \mathbf{K}_\xi^{(l)}) \right] \cdot (\xi \sigma_x, \sigma_y) \quad (\text{S18})$$

where $R(\varphi)$ is the 2×2 rotation matrix, v_F^{ml} is the monolayer Graphene Fermi velocity, and $\mathbf{K}_\xi^{(l)}$ is the Dirac point of layer l at valley ξ . The interlayer coupling is

$$U = \begin{pmatrix} u & u' \\ u' & u \end{pmatrix} + \begin{pmatrix} u & u'\nu^{-\xi} \\ u'\nu^\xi & u \end{pmatrix} e^{i\xi \mathbf{G}_1 \cdot \mathbf{r}} + \begin{pmatrix} u & u'\nu^\xi \\ u'\nu^{-\xi} & u \end{pmatrix} e^{i\xi(\mathbf{G}_2 + \mathbf{G}_3) \cdot \mathbf{r}} \quad (\text{S19})$$

Using minimal coupling, we obtain time-dependent monolayer graphene Hamiltonians, with Fourier transform

$$H_l^{(n)} = -\hbar v \left\{ R(l\theta/2) \left(\mathbf{k} + \frac{e}{\hbar} \frac{1}{2} \mathcal{E}[(\delta_{n,1} + \delta_{n,-1}) \hat{\mathbf{y}} - i(\delta_{n,-1} - \delta_{n,1}) \hat{\mathbf{x}}] - \mathbf{K}_\xi^{(l)} \right) \right\} \cdot (\xi \sigma_x, \sigma_y). \quad (\text{S20})$$

Then,

$$H_\xi^{(n)} = \begin{pmatrix} H_1^{(n)} & U^\dagger \delta_{n,0} \\ U \delta_{n,0} & H_2^{(n)} \end{pmatrix} \quad (\text{S21})$$

is the Fourier transform of the continuum model Hamiltonian. For the continuum model, we truncate the Floquet Hamiltonian (Eq. S16) to $-6 \leq m \leq 6$.

Upon diagonalizing the Floquet Hamiltonian, we obtain a large number of Floquet states per energy interval $[-\hbar\Omega/2, \hbar\Omega/2]$. We select two states per \mathbf{k} -point whose spectral weights $A_\alpha^0(\mathbf{k}) = |\langle \phi_{\mathbf{k}\alpha}^0 | \phi_{\mathbf{k}\alpha}^0 \rangle|^2$ are large (which makes their contribution to the Floquet-Boltzmann equation most important, see Sec. X).

C. Quasienergy Bands

In Sec. II, we provide and motivate the choices of physical parameters that we use in the main text. In Fig. S1, we preview the quasienergy bands for our choice of toy and continuum model parameters.

II. CHOICE OF PHYSICAL PARAMETERS

First, we present the physical parameters we use for the electronic Hamiltonian in the TBG continuum model (see Sec. IB for the Hamiltonian). We consider the non-interacting continuum model [3, 4] at a near-magic twist angle of $\theta = 1.13^\circ$. The bandwidth of the central bands at this angle is $W \approx 5$ meV, and a perturbative expansion of the Hamiltonian around the Brillouin zone Dirac points [4] estimates the Fermi velocity as

$$v_F(\theta) = v_F^{\text{ml}}(1 - 3\beta^2)/(1 + 3\beta^2(1 + \eta^2)), \quad (\text{S22})$$

where $\beta = u'/(\hbar k_\theta v_F^{\text{ml}})$ and $\eta = u/u'$ with $v_F^{\text{ml}} = 8 \times 10^5$ m/s, $k_\theta = 4\pi/(3L_M)$, $u = 0.0797$ eV, and $u' = 0.0975$ eV [3, 4]. Eq. S22 predicts that the Fermi velocity at the chosen twist angle is $v_F = 27$ km/s. However, the derivation of Eq. S22 approximates that $H_l^{(n)}$ is roughly θ -independent and tends to overestimate v_F (see Fig. 4 inset in [4]). We can obtain a better estimate by numerically calculating the Fermi velocity along the path K - M in \mathbf{k} -space of the $\nu = +1$ band in the $\xi = +1$ valley. (This is the direction of maximum Fermi velocity.) The estimate yields $v_F = 17.5$ km/s, and we hereafter use this value. In our Floquet Hamiltonian, we use a laser angular-frequency of $\Omega \approx W/\hbar \approx 5$ meV/ \hbar .

Second, we present the parameters we use for the electronic Hamiltonian of the TBG two-band toy tight binding model (see Sec. IA for the Hamiltonian). We choose our toy model Fermi velocity, frequency, and twist angle to roughly match those of the continuum model. Specifically, we use a twist angle of $\theta = 1.13^\circ$

and choose $W = 3.1$ meV so that the Fermi velocity $v_F = WL_M/(2\sqrt{3}\hbar) = 17$ km/s roughly matches that of the continuum model at the same angle. In the toy model Floquet Hamiltonian, we choose $\Omega \approx 5$ meV/ \hbar .

Third, we discuss the parameters we use for the TBG phonons. For both the continuum and toy models, we consider phonons speeds in the range of $c_{\text{ph}} \in [17.9 \text{ km/s}, 19.4 \text{ km/s}]$. In the toy model, $v_{\text{eff}}^0 = 18.9$ km/s, and, in the continuum model, $v_{\text{eff}}^0 = 19.5$ km/s, so the range of c_{ph} we choose covers the regime $c_{\text{ph}} < v_{\text{eff}}^0$, in which the drive induces the opposite regime $c_{\text{ph}} > v_{\text{eff}}(\mathcal{E})$ when $\mathcal{E} > \mathcal{E}^*$. We also use the same phonon bath temperature of $T_{\text{ph}} = 1$ K and Wannier orbital width $l_w = L_M/(5\sqrt{3})$ for the toy and continuum model calculations.

Please see Sec. X for details of the numerical \mathbf{k} -point grid.

III. ANOMALOUS HALL CONDUCTIVITY CALCULATIONS FOR THE CONTINUUM MODEL

In this section, we repeat the calculations in the main text on the TBG continuum model [3, 4]. We consider the non-interacting limit, setting $\epsilon \rightarrow \infty$ so that $I_{\mathbf{k}\alpha}^{\text{el-el}} = 0$.

First, we discuss differences in the bandstructure and topology at valleys $\xi = +1$ and $\xi = -1$. The circularly polarized laser opens a gap at the Dirac points, Δ_K , effectively adding a mass term $\xi\Delta_K\sigma_z$ to the Hamiltonian (see Sec. IB and [5] for a derivation) in the vicinity of the Dirac points. Because the sign of the mass term depends on ξ , the $\xi = \pm 1$ superlattice valley contributions to σ_{xy} do not trivially cancel to zero. In fact, in reciprocal space, the Berry curvature and occupations near

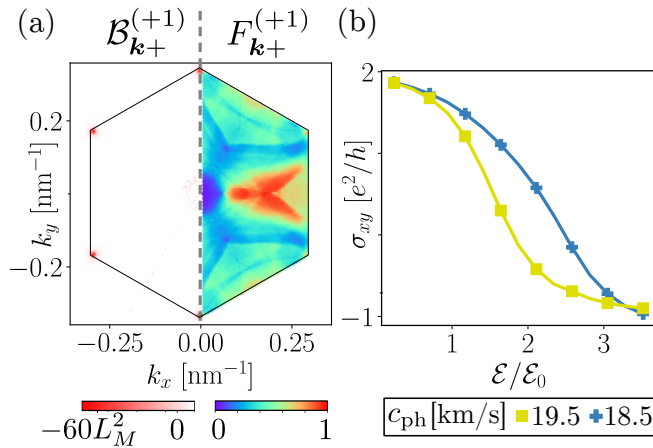


FIG. S2. (a) Left: the steady-state occupation of the upper Floquet band in valley $\xi = +1$ of the continuum model [3, 4]. Right: the Berry curvature of the same band, which peaks near the Dirac points and the resonance ring. (b) The anomalous Hall conductivity σ_{xy} as a function of drive strength \mathcal{E} .

$\xi = +1$ are simple $\pi/3$ rotations of those in $\xi = -1$, so

$$\sigma_{xy} = \frac{4e^2}{h} \sum_{\alpha=\pm} \int_{\text{MBZ}} \frac{d^2\mathbf{k}}{(2\pi)^2} \mathcal{B}_{\mathbf{k}\alpha}^{(+1)} F_{\mathbf{k}\alpha}^{(+1)}. \quad (\text{S23})$$

In Fig. S2, we show the steady-state and σ_{xy} for the continuum model calculation. Note that to simplify the calculations, we use the same effective form factor $\langle \xi\nu'\mathbf{k} + \mathbf{q} | \xi\nu\mathbf{k} \rangle \approx \delta_{\nu,\nu'} e^{-l_w^2 q^2/4}$ as the toy model.

IV. DIRECT VARIATION OF THE PHONON SPEED c_{ph}

Throughout the main text, we use the drive strength \mathcal{E} to control electron speeds. We could achieve similar results by keeping \mathcal{E} fixed and varying c_{ph} instead. Fig. S3 shows the variation of σ_{xy} as a function of c_{ph} . The curves resemble the dependence of σ_{xy} on \mathcal{E} in the main text (see, for e.g., Fig. 1(b)).

V. FORMAL DEFINITION, NUMERICAL EVALUATION, AND PHENOMENOLOGICAL MODEL OF \mathcal{A}_{in}

As described in the main text, an patch \mathcal{S}_{in} shaped as an elliptical annulus (see Fig. 3(a)) with area \mathcal{A}_{in} in momentum space vanishes as $\mathcal{E} \rightarrow \mathcal{E}^*$. Here, we provide a formal definition of \mathcal{A}_{in} and explain how we estimate its dependence on \mathcal{E} numerically and analytically.

A. Formal Definition

Let us first define \mathcal{A}_{in} formally. Consider a family of phonon cones centered throughout \mathcal{S}_K , the circular patch enclosing a K -point in the quasienergy spectrum (see Fig. 3(a)). Suppose that a subset of the phonon cones are centered throughout a small quasienergy window $d\epsilon_{\mathbf{k}+}$.

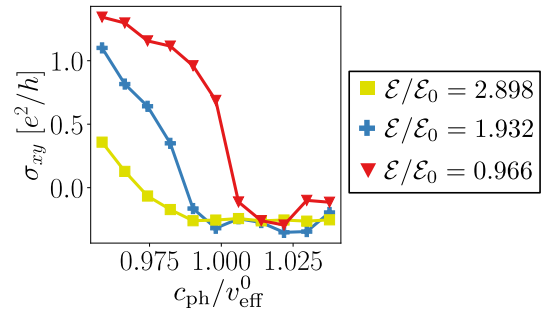


FIG. S3. Anomalous Hall conductivity of the toy model as a function of the ratio $c_{\text{ph}}/v_{\text{eff}}^0$ for three different drive field strengths $\mathcal{E}/\mathcal{E}_0$. The same electron-phonon decoupling process is visible as σ_{xy}^a plateaus.

The \mathbf{k} -space area of states $d\mathcal{A}_{\text{in}}$ containing intersections of the cones with the upper Floquet band is

$$d\mathcal{A}_{\text{in}} = d\varepsilon_{\mathbf{k}+} \sum_{s=\pm} \int d^2\mathbf{k}' \delta(\varepsilon_{\mathbf{k}+} - \varepsilon_{\mathbf{k}'+} + s\hbar c_{\text{ph}}|\mathbf{k}' - \mathbf{k}|). \quad (\text{S24})$$

Next, we integrate over $\varepsilon_{\mathbf{k}+}$ contained in \mathcal{S}_K to obtain

$$\begin{aligned} \mathcal{A}_{\text{in}} &= \int d\mathcal{A} = \int_{\mathbf{k} \in \mathcal{S}_K} d^2\mathbf{k} \frac{1}{D(\varepsilon_{\mathbf{k}+})} \times \\ &\times \left[\sum_{s=\pm} \int d^2\mathbf{k}' \delta(\varepsilon_{\mathbf{k}+} - \varepsilon_{\mathbf{k}'+} + s\hbar c_{\text{ph}}|\mathbf{k}' - \mathbf{k}|) \right], \end{aligned} \quad (\text{S25})$$

where

$$D(\varepsilon) = \sum_{\alpha} \int \frac{d^2\mathbf{k}}{(2\pi)^2} \delta(\varepsilon - \varepsilon_{\mathbf{k}\alpha}) \quad (\text{S26})$$

is the density of states in the quasienergy band structure. Exploiting the circular shape of \mathcal{S}_K ,

$$\int_{\mathbf{k} \in \mathcal{S}_K} d^2\mathbf{k} \approx \int d^2\mathbf{k} \Theta(|\mathbf{k} - \mathbf{K}| - k_p) \quad (\text{S27})$$

where k_p is the radius of the circular area \mathcal{A}_K of \mathcal{S}_K . Lastly, we calculate an approximate expression for k_p , the radius of \mathcal{A}_K . In the vicinity of the Dirac cone, the Hamiltonian is

$$H_K(\mathbf{k}, t) = \mathbf{d} \cdot \boldsymbol{\sigma}, \quad (\text{S28})$$

where $\mathbf{d} = \hbar v_F \xi k_x \hat{\mathbf{x}} + \hbar v_F \xi k_y \hat{\mathbf{y}} + \xi \Delta_K \mathcal{E}^2 \hat{\mathbf{z}}$. (See Sec. VIII for a detailed derivation.) The \mathbf{z} -component of the Berry curvature is

$$\mathcal{B}_{k\alpha}^z = \alpha \frac{d_z}{2|\mathbf{d}|^3} = \alpha \xi \frac{\Delta_K}{[(\hbar v_F k)^2 + \Delta_K^2]^{3/2}} \quad (\text{S29})$$

where $d_z = \xi \Delta_K$. At the half-maximum, $\mathcal{B}_{k_p\alpha}^z = 0.5\mathcal{B}_{0\alpha}^z$, so

$$k_p = (2^{2/3} - 1)^{1/2} \frac{\Delta_K}{\hbar v_F}. \quad (\text{S30})$$

B. Numerical Estimate

To generate the values of \mathcal{A}_{in} we present in Fig. 3(b), we evaluate the integrals in Eq. S25 on a finite-sized grid of \mathbf{k} -points, smearing the step function by replacing $\Theta(|\mathbf{k} - \mathbf{K}| - k_p) \rightarrow [e^{(|\mathbf{k} - \mathbf{K}| - k_p)/\sigma_k} + 1]^{-1}$, where $\sigma_k = 2\pi/(L_M N)$ is the grid spacing between \mathbf{k} -points on an $N \times N$ Monkhorst-Pack grid (see Sec. X). Thus, we approximate

$$\begin{aligned} \mathcal{A}_{\text{in}} &\approx \sum_{\mathbf{k}} [e^{(|\mathbf{k} - \mathbf{K}| - k_p)/\sigma_k} + 1]^{-1} \frac{1}{D(\varepsilon_{\mathbf{k}+})} \times \\ &\times \left[\sum_{s=\pm} \sum_{\mathbf{k}'} \delta(\varepsilon_{\mathbf{k}+} - \varepsilon_{\mathbf{k}'+} + s\hbar c_{\text{ph}}|\mathbf{k}' - \mathbf{k}|) \right]. \end{aligned} \quad (\text{S31})$$

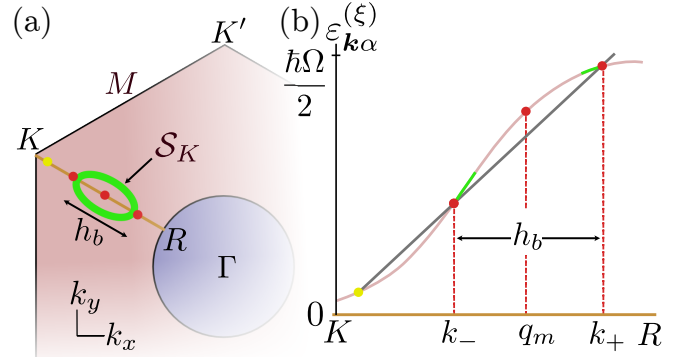


FIG. S4. (a) The intersection \mathcal{S}_K (Fig. 3(a)) as viewed on the Brillouin zone. The outer radius along the path KR is $h_b(\mathcal{E})$. (b) Quasienergy (pink) along the path KR , with the phonon light cone (grey) that determines the outer radius of \mathcal{A}_{in} . The intersections k_+ and k_- between the cone and the upper Floquet band determines $h_b(\mathcal{E}) = k_+ - k_-$.

For more information on how we approximate the Dirac Delta function on the grid, please see Sec. XA.

C. Phenomenological Model

In this section, we prove that the intersection area $\mathcal{A}_{\text{in}} \propto \max(\mathcal{E}^* - \mathcal{E}, 0)$ as $\mathcal{E} \rightarrow \mathcal{E}^*$. The shape of \mathcal{A}_{in} is an elliptical annulus as shown in Fig. 3(a). Let us use $h_b(\mathcal{E})$ and $w_b(\mathcal{E})$ respectively to denote the outer major and minor axis radii of the elliptical annulus (see Figs. S4(a) and S5(a)). In the following sections, we begin by generating analytical estimates of $h_b(\mathcal{E})$ and $w_b(\mathcal{E})$.

1. Estimate of h_b

First, let us consider a slice of the upper Floquet band in \mathbf{k} -space from the K to the resonance ring (R) along the direction of $h_b(\mathcal{E})$, as we show in Fig. S4(b). Let us define a one-dimensional momentum component q along the path K -R. We sketch a phonon light cone (grey) originating from a point (yellow) in \mathcal{S}_K that determines the outer radius of \mathcal{A}_{in} . The phonon cone intersects with the quasienergy at points k_+ and k_- , and the outer radius of \mathcal{A}_{in} is therefore $h_b(\mathcal{E}) = k_+ - k_-$. First, consider the undriven limit $\mathcal{E} = 0$, where the gaps $\Delta_R = 0$ and $\Delta_K = 0$. We choose some point q_m such that $k_- < q_m < k_+$ and series expand the energy $E(q)$ of the undriven system around q_m :

$$\begin{aligned} E(q) &\approx E(q_m) + E'(q_m)(q - q_m) + \frac{1}{2}E''(q_m)(q - q_m)^2 \\ &= a_2 q^2 + a_1 q + a_0, \end{aligned} \quad (\text{S32})$$

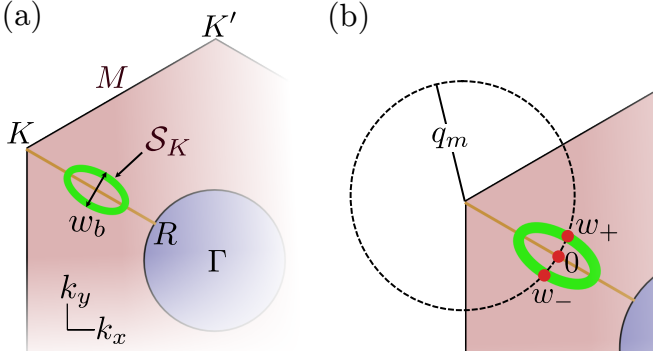


FIG. S5. (a) Width of the intersection \mathcal{S}_K , $w_b(\mathcal{E})$. (b) Circular coordinate system with arc length w (increasing counterclockwise) that we use to determine $w_b(\mathcal{E}) = w_+ - w_-$.

where $a_2 = E''(q_m)/2$, $a_1 = E'(q_m) - E''(q_m)q_m$, and $a_0 = E(q_m) - E'(q_m)q_m + E''(q_m)q_m^2/2$. As we increase \mathcal{E} , the gaps Δ_K and Δ_R widen. Let us write the quasienergy in the vicinity of q_m as

$$\varepsilon(q) \approx f(\mathcal{E})E(q) + \frac{\Delta_K}{2} \quad (\text{S33})$$

where $f(\mathcal{E}) \leq 1$ is a scaling factor that decreases as \mathcal{E} increases and accounts for band flattening due to Δ_K and Δ_R . Let

$$f^{-1} = 1 - b_1\tilde{\mathcal{E}} - b_2\tilde{\mathcal{E}}^2, \quad (\text{S34})$$

where $b_1 \geq 0$ and $b_2 \geq 0$ are constants dependent on the exact bandstructure (i.e., how the widening of Δ_K and Δ_R with \mathcal{E} affects the bandstructure near q_m). The roots of the equation $E(q) = \Delta_K/2 + \hbar c_{\text{ph}}q$ are k_{\pm} , and we may write the equation as

$$a_2q^2 + a_1q + a_0 = f\hbar c_s q, \quad (\text{S35})$$

from which we find that

$$h_b = k_+ - k_- = \sqrt{(a_1 - f\hbar c_s)^2 - 4a_2a_0}. \quad (\text{S36})$$

Solving for \mathcal{E}^* through the equation $h_b = 0$, and then series expanding the expression $(a_1 - f\hbar c_s)^2 - 4a_2a_0$ in powers of small $\mathcal{E} - \mathcal{E}^*$, we find that $(a_1 - f\hbar c_s)^2 - 4a_2a_0 \sim \mathcal{E}^* - \mathcal{E}$, so $h_b \sim \sqrt{\mathcal{E}^* - \mathcal{E}}$.

2. Estimate of w_b

To estimate w_b (see Fig. S5(a)), we define a circular coordinate system shown in Fig. S5(b) whose origin is the K point and arc length w is zero along the KR slice, increasing counterclockwise. The quasienergy $\varepsilon(w)$ along the circle perimeter varies with w ; let us approximate

$$\varepsilon(w) \approx \hbar\Omega/2 - (d_0 + d_2w^2), \quad (\text{S37})$$

using some fitting parameters d_0 and d_2 . (We assume that $w = 0$ is at local maximum of $\varepsilon(w)$, so there is no linear term in Eq. S37.) Roughly, $w_b = w_+ - w_-$, where we find w_+ and w_- by finding the roots of the equation

$$\hbar\Omega/2 - \Delta(w) = f\hbar c_s q_m. \quad (\text{S38})$$

Here, once again, we use the factor f in Eq. S34 to account for band flattening as \mathcal{E} increases from zero. So,

$$w_b = w_+ - w_- = 2\sqrt{(f\hbar c_s q_m + \hbar\Omega/2 - d_0)/d_2}. \quad (\text{S39})$$

Solving for \mathcal{E}^* by setting $w_b = 0$ and series expanding $f\hbar c_s q_m + \hbar\Omega/2 - d_0$ in powers of \mathcal{E} , we find that $w_b \sim \sqrt{\mathcal{E}^* - \mathcal{E}}$.

3. Estimate of \mathcal{A}_{in}

In the limit $\mathcal{E} \rightarrow \mathcal{E}^*$, the elliptical annulus with finite thickness collapses into a filled ellipse. Thus, in the limit $\mathcal{E} \rightarrow \mathcal{E}^*$, we estimate that $\mathcal{A}_{\text{in}} = \pi h_b(\mathcal{E})w_b(\mathcal{E}) \propto \max(\mathcal{E}^* - \mathcal{E}, 0)$.

VI. PREDICTING \mathcal{E}^* FOR THE TOY MODEL

Here, we use the quasienergy dispersion of the toy model to predict \mathcal{E}^* . By writing an approximate, analytic expression for $v_{\text{eff}}(\mathcal{E})$ (see Eq. 6), we can find \mathcal{E}^* using the relation $v_{\text{eff}}(\mathcal{E}^*) = c_{\text{ph}}$.

From Eq. 6, $v_{\text{eff}}(\mathcal{E}) = (\varepsilon_{\mathbf{k}^*+} - \varepsilon_{\mathbf{K}+})/|\mathbf{k}^* - \mathbf{K}|$ for some appropriately-chosen \mathbf{k}^* (dropping the superlattice valley index for notational simplicity). One can find numerically that \mathbf{k}^* does not shift significantly with Ω or \mathcal{E} . We write an ansatz

$$\varepsilon_{\mathbf{k}^*+} \approx \hbar v_{\text{eff}}^0 |\mathbf{k}^* - \mathbf{K}| - \frac{\hbar v_F}{L_M} \left(f'_1 \tilde{\mathcal{E}} + f'_2 \tilde{\mathcal{E}}^2 \right) \frac{|\mathbf{k}^* - \mathbf{K}|}{\Omega/(2v_{\text{eff}}^0)}, \quad (\text{S40})$$

where f'_1 and f'_2 are fitting constants dependent on the quasienergy bandstructure. Here, $\hbar v_F/L_M$ is the order of magnitude energy scale of the resonance ring gap Δ_R . The dependence of $\varepsilon_{\mathbf{k}^*+}$ on \mathcal{E} arises predominantly from Δ_R . The dependence is stronger when \mathbf{k}^* is close to the resonance ring, and we encode this behavior in the ratio $|\mathbf{k}^* - \mathbf{K}|/\Omega/(2v_{\text{eff}}^0)$, where $\Omega/(2v_{\text{eff}}^0)$ is the \mathbf{k} -space distance between the K point and the resonance ring. Separately, we know that $\varepsilon_{\mathbf{K}+} = \Delta_K/2$. We use Eq. 6 to infer

$$v_{\text{eff}}^0(\mathcal{E}) = v_{\text{eff}}^0 - \frac{\Delta_K}{2\hbar|\mathbf{k}^* - \mathbf{K}|} - \frac{2\hbar v_F v_{\text{eff}}^0}{L_M \Omega} \left(f'_1 \tilde{\mathcal{E}} + f'_2 \tilde{\mathcal{E}}^2 \right). \quad (\text{S41})$$

We know that $v_{\text{eff}}^0 \propto v_F$. We also assume that $|\mathbf{k}^* - \mathbf{K}|$ does not change significantly with \mathcal{E} , so it is independent of the drive and only dependent on the superlattice scale:

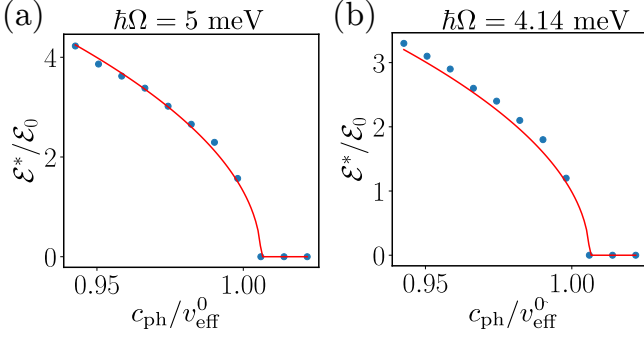


FIG. S6. Comparing numerical evaluation of \mathcal{E}^* (points) to an analytic fit to Eq. S44. We use the same fitting parameters $f_2 = 0.778$, $f_1 = 0$, and $\delta(N) = 0.006$ for both panels.

$|\mathbf{k}^* - \mathbf{K}| \propto L_M^{-1}$. Thus, we can absorb some unknown coefficients into new coefficients f_1'' and f_2'' to obtain

$$v_{\text{eff}}^0(\mathcal{E}) = v_{\text{eff}}^0 - \frac{\hbar v_F^2}{L_M \Omega} \left(f_1'' \tilde{\mathcal{E}} + f_2'' \tilde{\mathcal{E}}^2 \right). \quad (\text{S42})$$

Upon solving for $\tilde{\mathcal{E}}^*$ from $c_s = v_{\text{eff}}(\mathcal{E}^*)$, we find that

$$\tilde{\mathcal{E}}^* \approx \sqrt{\frac{L_M \Omega}{3 f_2 v_F}} \left(\sqrt{1 - c_{\text{ph}}/v_{\text{eff}}^0 + f_1^2 - f_1} \right), \quad (\text{S43})$$

where f_1 and f_2 are new, rescaled fitting constants. Using the relation $\tilde{\mathcal{E}} = e L_M \mathcal{E} / (\sqrt{3} \hbar \Omega)$, we find

$$\mathcal{E}^* \approx \frac{\hbar \Omega^{3/2}}{f_2 e L_M^{1/2} v_F^{1/2}} \left(\sqrt{1 - c_{\text{ph}}/v_{\text{eff}}^0 + f_1^2 - f_1} \right), \quad (\text{S44})$$

As $c_{\text{ph}} \rightarrow v_{\text{eff}}^0$, $\mathcal{E}^* \propto (1 - c_{\text{ph}}/v_{\text{eff}}^0)^\gamma$ where $\gamma = 1$ ($1/2$) if $f_1 \neq 0$ ($= 0$). See Fig. S6 for a fit for two different frequencies Ω .

Finite grid size effects on an $N \times N$ Monkhorst-Pack grid (see Sec. X) generate a small numerical error $\delta(N)$ that enters S44 as

$$\mathcal{E}^* \approx \frac{\hbar L_M^{1/2} \Omega^{3/2}}{f_2 e L_M v_F^{1/2}} \left(\sqrt{1 - c_{\text{ph}}/v_{\text{eff}}^0 + \delta(N) + f_1^2 - f_1} \right). \quad (\text{S45})$$

To see this, let us consider the details of the finite-sized grid. We impose energy conservation through a broadened Dirac Delta function (see Sec. X A), which we model as a Gaussian function in energy with a tiny width

$$\sqrt{2}\sigma \approx 0.1 \cdot \sqrt{2} \cdot \frac{W}{2N/3}. \quad (\text{S46})$$

(We motivate the choice of the prefactor of 0.1 in Sec. X A.) Since we avoid the high symmetry K point in our grids, the \mathbf{k} -point with largest Berry curvature is, in fact, a point \mathbf{k}_{near} point shifted away from K by a small distance in momentum space of

$$|\delta \mathbf{k}| = |\mathbf{k}_{\text{near}} - \mathbf{K}| \approx \frac{1}{2} \frac{\Omega / (2 \hbar v_{\text{eff}}^0)}{2N/3} = \frac{\Omega}{4 v_{\text{eff}}^0 (2N/3)}. \quad (\text{S47})$$

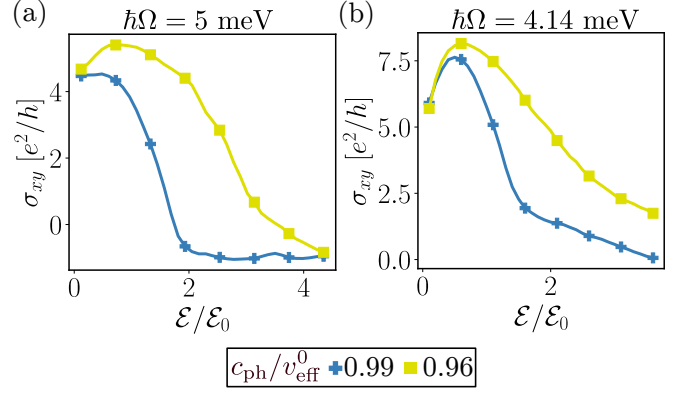


FIG. S7. Comparing the dependence of σ_{xy} on \mathcal{E} for (a) the frequency considered in the main text and (b) a lower frequency where Floquet-Umklapp processes are stronger. Note that the frequency in panel (b) is inaccessible without generating two-photon resonances in the continuum model due to the peaked shape of the $\nu = \pm 1$ bands near the Γ point.

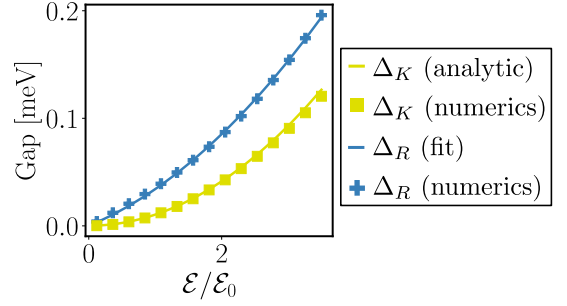


FIG. S8. Comparison of the fitted Δ_R and predicted Δ_K in Equations S51 and S55 (solid lines) to those obtained from numerics (points), using $\hbar\Omega = 5$ meV in the toy model. Here, we fit Δ_R with factors of $f_1^R = 0.04$ and $f_2^R = 0.0184$ (see Eq. S51).

This point is shifted in quasienergy by $\hbar v_F |\delta \mathbf{k}|$ relative to the actual K point. We can account for both of these effects by shifting $\varepsilon_{\mathbf{K}+} \rightarrow \varepsilon_{\mathbf{K}+} + \delta \varepsilon$, with $\delta \varepsilon = \sqrt{2}\sigma + \hbar v_F |\delta \mathbf{k}|$ and solve $v_{\text{eff}}(\mathcal{E}^*) = c_{\text{ph}}$ to find Eq. S45 with $\delta(N) = \delta \varepsilon / (\hbar v_{\text{eff}}^0 |\mathbf{k}^* - \mathbf{K}|)$.

VII. DIFFERENT FREQUENCIES

Reducing Ω below the value considered above will increase the ratio $(v_F e \mathcal{E} / \Omega^2)^2$ and in turn strengthen Floquet Umklapp processes, modifying the shape of the σ_{xy} curve. We demonstrate this in Fig. S7(b) for an angular frequency $\Omega = 4.135$ meV/ \hbar . However, such a low-frequency regime is inaccessible in the continuum model (without generating two-photon resonances) due to the peaked shape of the continuum model $\nu = \pm 1$ band near the Γ point, so we do not consider this lower (doubly-resonant) frequency regime in the main text.

VIII. GAP SIZES

In this section, we estimate the size of the Floquet-induced gaps Δ_K and Δ_R . By the rotating wave approximation, the Floquet-induced gap at the resonance ring, Δ_R , is roughly proportional to the drive energy [6]. For a resonant drive that couples electronic states near the Dirac points, the drive energy is roughly

$$v_F e A / \hbar, \quad (\text{S48})$$

as predicted by minimal coupling $\mathbf{q} \rightarrow \mathbf{q} + e\mathbf{A}(t)/\hbar$ in the Dirac cone Hamiltonian

$$H_K(\mathbf{q}) = \hbar v_F \mathbf{q} \cdot (\xi \sigma_x, \sigma_y) \quad (\text{S49})$$

with $v_F = WL_M/(2\sqrt{3}\hbar)$. (We always use perturbative drives that generally fall in the range of $\tilde{\mathcal{E}} < 1$.) We expect that

$$\Delta_R \approx \frac{\hbar v_F}{L_M} \tilde{\mathcal{E}}. \quad (\text{S50})$$

Such an approximation works well for low-frequency resonant drives that couple states near the Dirac points. However, resonant drives with higher frequencies, like those used in the main text, couple states closer to the Γ -points of the TBG energy dispersion where the bands are nonlinear in q . In such a case, higher order (e.g., $O(\tilde{\mathcal{E}}^2)$) contributions (from $O(q^2)$ contributions of the band-structure) to Δ_R become dominant. In the present example, the energy of the tight binding model for graphene is quadratic in momentum near the Γ point, so we write an ansatz

$$\Delta_R \approx \frac{\hbar v_F}{L_M} (f_1^R \tilde{\mathcal{E}} + f_2^R \tilde{\mathcal{E}}^2), \quad (\text{S51})$$

and fit f_1^R and f_2^R to match Δ_R obtained by numerically diagonalizing the Floquet Hamiltonian, as shown in Fig. S8.

We can estimate the Floquet-induced K -point gap, Δ_K , by considering the time-dependent Dirac Hamiltonian

$$H_K(\mathbf{q}, t) = \hbar v_F (\xi q_x \sigma^x + q_y \sigma^y) + v_F e A [\xi \cos(\Omega t) \sigma^x - \sin(\Omega t) \sigma^y]. \quad (\text{S52})$$

and performing a Van Vleck expansion [6–8] to obtain an effective Floquet Hamiltonian

$$H_{K,\text{eff}}(\mathbf{q}) = H_K^{(0)} + \frac{[H_K^{(-1)}, H_K^{(1)}]}{\hbar \Omega} = H_K + \xi \frac{e^2 v_F^2 A^2}{\hbar \Omega} \sigma^z \quad (\text{S53})$$

with

$$H_K^{(n)}(\mathbf{q}) = \frac{1}{2\pi/\Omega} \int_0^{2\pi/\Omega} H_K(\mathbf{q}, t) e^{-in\Omega t} dt. \quad (\text{S54})$$

From Eq. S53, we can extract

$$\Delta_K = \frac{2e^2 v_F^2}{\hbar \Omega} A^2 = \frac{6\hbar v_F^2}{L_M^2 \Omega} \tilde{\mathcal{E}}^2. \quad (\text{S55})$$

IX. FLOQUET BOLTZMANN EQUATION

Here, we present the full expression for the Floquet-Boltzmann equation [9], which we copy below for convenience:

$$\partial_t F_{\mathbf{k}\alpha}(t) = I_{\mathbf{k}\alpha}^{\text{el-ph}}[\{F_{\mathbf{k}\alpha}(t)\}] + I_{\mathbf{k}\alpha}^{\text{el-el}}[\{F_{\mathbf{k}\alpha}(t)\}]. \quad (\text{S56})$$

The electron-phonon collision integral is

$$\begin{aligned} I_{\mathbf{k}\alpha}^{\text{el-ph}}[\{F_{\mathbf{k}\alpha}\}] &= \frac{2\pi}{\hbar} \sum_{\mathbf{k}' \in \text{BZ}} \sum_{\alpha'} \sum_j \sum_n |\mathcal{G}_{\mathbf{k}\alpha}^{\mathbf{k}'\alpha'}(n, j)|^2 \\ &\times \left[\{F_{\mathbf{k}'\alpha'}(1 - F_{\mathbf{k}\alpha}) \mathcal{N}(\hbar\omega_j(\mathbf{k}' - \mathbf{k})) - F_{\mathbf{k}\alpha}(1 - F_{\mathbf{k}'\alpha'})[1 + \mathcal{N}(\hbar\omega_j(\mathbf{k}' - \mathbf{k}))]\} \right. \\ &\quad \times \delta(\varepsilon_{\mathbf{k}'\alpha'} - \varepsilon_{\mathbf{k}\alpha} + \hbar\omega_j(\mathbf{q}) + n\hbar\Omega) \\ &\quad \left. + \{F_{\mathbf{k}'\alpha'}(1 - F_{\mathbf{k}\alpha})[1 + \mathcal{N}(\hbar\omega_j(\mathbf{k}' - \mathbf{k}))] - F_{\mathbf{k}\alpha}(1 - F_{\mathbf{k}'\alpha'}) \mathcal{N}(\hbar\omega_j(\mathbf{k}' - \mathbf{k}))\} \right. \\ &\quad \left. \times \delta(\varepsilon_{\mathbf{k}'\alpha'} - \varepsilon_{\mathbf{k}\alpha} - \hbar\omega_j(\mathbf{q}) + n\hbar\Omega) \right] \end{aligned} \quad (\text{S57})$$

$$\mathcal{G}_{\mathbf{k}\alpha}^{\mathbf{k}'\alpha'}(n, j) = \sum_{\nu} \frac{1}{\sqrt{A_{\text{Moiré}}}} \frac{D}{\sqrt{2\rho c_{\text{ph}}}} \sqrt{\hbar\omega_j(\mathbf{k}' - \mathbf{k})} e^{-|\mathbf{k}' - \mathbf{k} + \mathbf{G}_j|^2 l_w^2/4} \sum_m \langle \phi_{\mathbf{k}'\alpha'}^{n+m} | \nu \mathbf{k}' \rangle \langle \nu \mathbf{k} | \phi_{\mathbf{k}\alpha}^m \rangle \quad (\text{S58})$$

where $\rho = 1.52 \times 10^{-6}$ kg/m² is the 2D density of the graphene layers, D is the deformation potential, and the

acoustic phonon mode j has frequency $\omega_j(\mathbf{q}) = \hbar c_{\text{ph}} |\mathbf{q} + \mathbf{G}_j|$ with $\{\mathbf{G}_j\}$ being the set of all possible reciprocal

lattice vectors. The function $\mathcal{N}(\varepsilon) = (e^{-\varepsilon/k_B T_{\text{ph}}} - 1)^{-1}$ is the Bose-Einstein occupation of the phonon bath at

temperature T_{ph} . The electron-electron collision integral is

$$I_{\mathbf{k}\alpha}^{\text{el-el}}[\{F_{\mathbf{k}\alpha}\}] = \frac{4\pi}{\hbar} \frac{1}{N^2} \sum_{\mathbf{k}_2 \in \text{BZ}} \sum_{\mathbf{k}_3 \in \text{BZ}} \sum_{\alpha_2, \alpha_3, \alpha_4} \sum_n \sum_{\mathbf{G}} |\mathcal{V}_{(\mathbf{k}, \alpha), (\mathbf{k}_2, \alpha_2)}^{(\mathbf{k}_3, \alpha_3), (\mathbf{k}_1 + \mathbf{k}_2 - \mathbf{k}_3, \alpha_4)}(n, \mathbf{G})|^2 \times \quad (\text{S59})$$

$$\times \delta(\varepsilon_{\mathbf{k}\alpha} + \varepsilon_{\mathbf{k}_2\alpha_2} - \varepsilon_{\mathbf{k}_3\alpha_3} - \varepsilon_{\mathbf{k} + \mathbf{k}_2 - \mathbf{k}_3, \alpha_4} + n\hbar\Omega) \times$$

$$\times [(1 - F_{\mathbf{k}\alpha})(1 - F_{\mathbf{k}_2\alpha_2})F_{\mathbf{k}_3\alpha_3}F_{\mathbf{k}_1 + \mathbf{k}_2 - \mathbf{k}_3, \alpha_4} - F_{\mathbf{k}\alpha}F_{\mathbf{k}_2\alpha_2}(1 - F_{\mathbf{k}_3\alpha_3})(1 - F_{\mathbf{k}_1 + \mathbf{k}_2 - \mathbf{k}_3, \alpha_4})]$$

$$\mathcal{V}_{(\mathbf{k}, \alpha), (\mathbf{k}_2, \alpha_2)}^{(\mathbf{k}_3, \alpha_3), (\mathbf{k}_1 + \mathbf{k}_2 - \mathbf{k}_3, \alpha_4)}(n) = \sum_{\nu_1, \nu_2} \sum_{\nu_3, \nu_4} \sum_{n_2, n_3, n_4} V(\mathbf{k}_2 - \mathbf{k}_3 + \mathbf{G}) e^{-|\mathbf{q} + \mathbf{G}|^2 l_w^2 / 2} \delta_{\nu_1, \nu_3} \delta_{\nu_2, \nu_4} \langle \phi_{\mathbf{k}\alpha}^{n - n_2 + n_3 + n_4} | \nu_1 \mathbf{k} \rangle \langle \phi_{\mathbf{k}_2\alpha_2}^{n_2} | \nu_2 \mathbf{k}_2 \rangle \times \quad (\text{S60})$$

$$\times \langle \nu_3 \mathbf{k}_3 | \phi_{\mathbf{k}_3\alpha_3}^{n_3} \rangle \langle \nu_4 \mathbf{k}_4 | \phi_{\mathbf{k} + \mathbf{k}_2 - \mathbf{k}_3, \alpha_4}^{n_4} \rangle.$$

We solve for $\partial_t F_{\mathbf{k}\alpha} = 0$ using the Newton-Raphson algorithm. To ensure charge neutrality, we add a Lagrange multiplier term $\lambda(\sum_{\mathbf{k}\alpha} F_{\mathbf{k}\alpha} - N)$ to the Floquet-Boltzmann equation, choosing some large constant λ .

X. MONKHORST-PACK GRID, NUMERICAL INTEGRATION, AND CONVERGENCE

In this section, we describe the methods we use to discretize the momentum Brillouin zone. We perform the Boltzmann equation integrals, introduced in Equations S57 and S59, over an $N \times N$ Monkhorst-Pack (MP) set of grid points [10], with \mathbf{k} -points

$$\mathbf{k}_{m,n} = \frac{m\mathbf{G}_1 + n\mathbf{G}_2}{N}, \quad (\text{S61})$$

odd N , and $m, n = 0, \dots, N - 1$. Specifically, we avoid values of $N(\text{mod } 3) = 0$ that generate a \mathbf{k} -point exactly at the high-symmetry point of K , because such grids converge poorly when the drive strength is weak and Floquet-induced gap Δ_K is small.

A. Energy and Momentum Conservation

Here, we discuss in detail how we impose momentum and energy conservation on this MP grid. The space of MP \mathbf{k} vectors are closed under addition and subtraction (modulo a reciprocal lattice vector), so conservation of momentum (e.g., $\mathbf{k} + \mathbf{k}_2 - \mathbf{k}_3$ in Eq. S59), is simple to implement. We impose energy conservation via a smeared Dirac Delta function

$$\delta(\varepsilon) = \begin{cases} 1.04766e^{-\varepsilon^2/2\sigma^2}/(2.5066283\sigma), & \text{if } |\varepsilon| < 2\sigma, \\ 0, & \text{otherwise,} \end{cases} \quad (\text{S62})$$

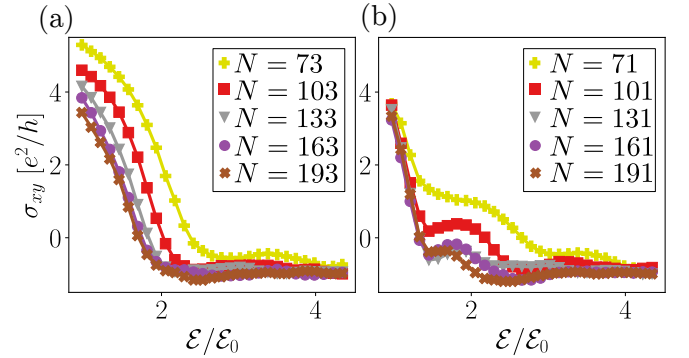


FIG. S9. Convergence of anomalous conductivity with grid size for (a) $N(\text{mod } 3) = 1$ and (b) $N(\text{mod } 3) = 2$. Due to the positioning of grid points near the K point, the results at low grid resolutions show significant disagreement. Here, $\varepsilon_0 = 4.41 \times 10^4$ V/m.

where we have chosen numerical factors so that

$$\int_{-\infty}^{\infty} \delta(\varepsilon) d\varepsilon = 1. \quad (\text{S63})$$

The smearing parameter σ is one-tenth of the maximum quasienergy spacing between nearest-neighbor MP \mathbf{k} -points

$$\sigma = 0.1 \max_{\langle \mathbf{k}, \mathbf{k}' \rangle, \alpha} |\varepsilon_{\mathbf{k}\alpha}^{(\xi)} - \varepsilon_{\mathbf{k}'\alpha}^{(\xi)}|, \quad (\text{S64})$$

where $\langle \mathbf{k}, \mathbf{k}' \rangle$ restricts \mathbf{k}' to be a nearest-neighbor of \mathbf{k} , and we have tuned the prefactor of 0.1 so that upon calculating the steady-state without Floquet-Umklapp processes, we obtain a Fermi-Dirac distribution, $F_{\mathbf{k}\alpha}^{(\xi)} = (e^{\varepsilon_{\mathbf{k}\alpha}/k_B T_{\text{ph}}} + 1)^{-1}$ with temperature T_{ph} of the phonon bath [11].

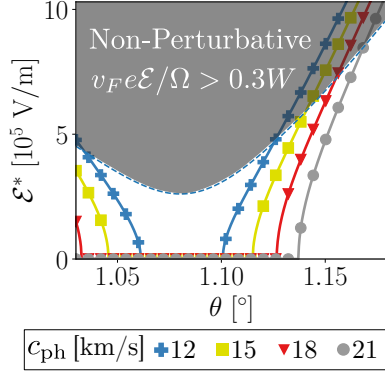


FIG. S10. The requirement that the laser drive strength \mathcal{E} is perturbative, i.e. a fraction of electron bandwidth $e\mathcal{E}L_M < W$, narrows the range of \mathcal{E} values that can be used. As a result, the range of c_{ph} whose \mathcal{E}^* is visible is limited as well - we postulate that they are pushed to higher drive strengths \mathcal{E} .

B. Convergence of Conductivities

In Fig. S9, we show the convergence of the Hall conductivity σ_{xy} with grid size, using $\hbar\Omega = 5$ meV. In the main text, we use a 163×163 MP grid for non-interacting calculations, and a 73×73 grid for interacting calculations.

XI. BERRY CURVATURE CALCULATIONS

We follow the Berry curvature calculation presented in [12], defining U(1) link variables

$$U_\mu(\mathbf{k}, t) = \frac{\langle \alpha(\mathbf{k}, t) | \alpha(\mathbf{k} + \hat{\mu}, t) \rangle}{|\langle \alpha(\mathbf{k}, t) | \alpha(\mathbf{k} + \hat{\mu}, t) \rangle|} \quad (\text{S65})$$

where $\mu = x, y$, $\hat{\mu} = \mathbf{G}_\mu / N$, and $|\alpha(\mathbf{k}, t)\rangle$ are the Bloch vectors (i.e., $|\psi_{\mathbf{k}\alpha}(t)\rangle = e^{-i\mathbf{k}\cdot\mathbf{r}}|\alpha(\mathbf{k}, t)\rangle$). The Berry curvature is

$$\mathcal{B}_{\mathbf{k}\alpha}(t) = \frac{(2\pi)^2}{N^2 A_M} \arg \left[\frac{U_x(\mathbf{k}, t) U_y(\mathbf{k} + \hat{x}, t)}{U_x(\mathbf{k} + \hat{y}, t) U_y(\mathbf{k}, t)} \right] \quad (\text{S66})$$

and we use the time-averaged Berry curvature

$$\mathcal{B}_{\mathbf{k}\alpha} \equiv \frac{1}{2\pi/\Omega} \int_0^{2\pi/\Omega} \mathcal{B}_{\mathbf{k}\alpha}(t) dt \quad (\text{S67})$$

in transport calculations.

XII. THE PERTURBATIVE REGIME AT DIFFERENT TWIST ANGLES

We have treated the laser drive as a perturbation to the undriven TBG Hamiltonian, which restricts the range of field strengths \mathcal{E} we can use to a weak perturbative

regime. This also narrows the range of phonon speeds c_{ph} that will generate a critical field strength \mathcal{E}^* in the perturbative regime, hence the narrow range of c_{ph} we have considered in, e.g., Fig. 1(c). For various twist angles, we estimate the range of drive strengths \mathcal{E} that are perturbative in the unshaded region of Fig. S10 and overlap in solid lines the predicted value of \mathcal{E}^* for different speeds of sound. The shaded, non-perturbative regime corresponds to drive energy scales $v_F e \mathcal{E} / \Omega$ greater than a fraction, e.g., 0.3, of the bandwidth W . Here, we follow the analysis in [4] to estimate the undriven Fermi velocity

$$v_F(\theta) = \sqrt{\left((1 - 3\alpha^2) / (1 + 3\alpha^2(1 + \eta^2)) \times v_F^{\text{ml}} \right)^2 + v_{\text{min}}^2}, \quad (\text{S68})$$

where $v_{\text{min}} = 10^4$ m/s is a manually set minimum Fermi velocity of the undriven flat bands, and we use the same parameters as in Sec. II. We also adjust Ω such that $\Omega/v_F(\theta)$ is constant and equal to those considered in Figs. 1-4.

-
- [1] M. S. Rudner and N. H. Lindner, “The floquet engineer’s handbook,” (2020), [arXiv:2003.08252 \[cond-mat\]](https://arxiv.org/abs/2003.08252).
 - [2] Q. Chen, L. Du, and G. A. Fiete, *Phys. Rev. B* **97**, 035422 (2018).
 - [3] M. Koshino, N. F. Q. Yuan, T. Koretsune, M. Ochi, K. Kuroki, and L. Fu, *Phys. Rev. X* **8**, 031087 (2018).
 - [4] R. Bistritzer and A. Macdonald, *Proceedings of the National Academy of Sciences of the United States of America* **108** (2010), 10.1073/pnas.1108174108.
 - [5] O. Katz, G. Refael, and N. H. Lindner, *Phys. Rev. B* **102**, 155123 (2020).
 - [6] M. Rudner and N. Lindner, *Nature Reviews Physics* **2**, 1 (2020).
 - [7] M. Rodriguez-Vega, M. Vogl, and G. Fiete, *Annals of Physics* **435**, 168434 (2021).
 - [8] T. Kitagawa, T. Oka, A. Brataas, L. Fu, and E. Demler, *Phys. Rev. B* **84**, 235108 (2011).
 - [9] K. I. Seetharam, C.-E. Bardyn, N. H. Lindner, M. S. Rudner, and G. Refael, *Phys. Rev. B* **99**, 014307 (2019).
 - [10] H. J. Monkhorst and J. D. Pack, *Phys. Rev. B* **13**, 5188 (1976).
 - [11] V. M. Galitskii and V. F. Elesin, *Journal of Experimental and Theoretical Physics* **30** (1970).
 - [12] T. Fukui, Y. Hatsugai, and H. Suzuki, *Journal of the Physical Society of Japan* **74**, 1674 (2005), <https://doi.org/10.1143/JPSJ.74.1674>